POLITECNICO
MILANO 1863

Department of mechanical engineering

Doctoral programme in mechanical engineering

Thermally controlled microbalance for contamination monitoring

Doctoral dissertation of:
Marianna Magni

Supervisor:
Prof. Bortolino Saggin

Tutor:
Prof. Stefano Bruni

The chair of the doctoral program:
Prof. Daniele Rocchi

2018-PhD cycle XXXI

‘Dobbiamo trovare il tempo per fermarci

e ringraziare le persone che fanno la differenza nelle nostre vite’

(John F. Kennedy)

A Federica

‘Nulla si crea, nulla si distrugge, tutto si trasforma’

(Antoine-Laurent de Lavoisier)

Abstract

This research is focused on a new type of Quartz Crystal Microbalance devoted to the monitoring of contaminants. The innovative features of this instrument are related to its thermal control. Two film resistors deposited around the electrodes allows measuring directly the crystal temperature and at the same time delivering on the crystal the power for thermal control. This new crystal configuration combines with a new supporting system allowing for a rigid but kinematic mounting and to achieve when needed the thermal insulation of the crystal. The innovative thermal system allows achieving high temperatures with low power consumption, to control the crystal temperature with unprecedented accuracy, to perform fast heating cycles reducing the time required for thermo-gravimetric analysis. The new thermal configuration determines also different temperature fields on the crystal and the main objective of this work is the analysis of the effects of temperature on the new quartz crystal microbalance for thermogravimetric analyses in space. Significant temperature gradients are expected on the crystal because of the built-in heater whose layout is constrained due to the electrodes pattern; this forces to quite high specific power dissipations because the required power must be localized on the very small area of the heater film. As result, along with the temperature (T) also the thermal gradients (ΔT) will have to be compensated during TGA. The accuracy of the temperature measurement of the QCM is crucial because it is well known that the oscillating frequency of the crystal strongly depends on its temperature. A relevant portion of the work has been therefore devoted to the calibration of the QCM thermometers and the assessment the achievable measurement accuracy.

The accurate crystal temperature measurement allowed also for an accurate determination of the frequency-temperature relationship. The comparison between the frequency changes in case of uniform temperature and those observed while using the crystal heaters has proved that the temperature gradients have a strong effect on the crystal frequency.

To identify the temperature field on the crystal surface of a standard QCM crystal, a thermal image processing and the thermal model have been developed. The model has been firstly validated by comparing the predicted temperatures with those measured through a thermal mapper. Once validated the thermal model has been used to evaluate the temperature gradients on different crystals and for different input power. In order to correlate the temperature gradient with the frequency variation, a test campaign has been performed measuring the frequency changes deriving from different power levels on the crystal heaters. In parallel, using the validated thermal model, the power dissipations and boundary conditions applied in the experimental activity, have been used as inputs for the thermal analysis, assessing the temperature gradients under the same conditions. From this test campaign and thermal analysis, the effect of the thermal gradient has been assessed. The frequency changes proved to be accurately represented by a third order polynomial of the average thermal gradient. Eventually having characterized both the effect of the average temperature and of the thermal gradient a correction procedure of the temperature effects has been implemented. The validation of the correction procedure was carried-out with a new test campaign evidencing that residual errors lower than 7% were achieved. The correction procedure therefore, despite being only a first step that can be further improved

with testing in high vacuum to avoid the effects of contaminants and on a wider range of conditions to assess repeatability and robustness, is promising especially for application of the QCM in high temperature TGA.

Keywords: QCM; thermal gradient; thermal analysis; quartz crystal; piezoelectric effect; thermo-elastic stress; natural frequency; mass measurement; condensation; TGA.

Sommario

L’attività di ricerca si concentra su un nuovo tipo di microbilancia a cristallo di quarzo utilizzata per il monitoraggio dei contaminanti. Le caratteristiche innovative di questo strumento sono legate al suo controllo termico. Due resistenze a film depositate attorno agli elettrodi consentono di misurare direttamente la temperatura del cristallo e allo stesso tempo di fornire sul cristallo la potenza per il controllo termico. Questa nuova configurazione del cristallo si combina con un nuovo sistema di supporto che consente un montaggio rigido ma cinematico e di ottenere, quando necessario, l'isolamento termico del cristallo. L'innovativo sistema termico consente di raggiungere temperature elevate con un basso consumo energetico, di controllare la temperatura del cristallo con una precisione senza precedenti, di eseguire cicli di riscaldamento rapidi riducendo il tempo richiesto per l'analisi termo-gravimetrica. La nuova configurazione termica determina anche diversi campi di temperatura sul cristallo e l'obiettivo principale di questo lavoro è l'analisi degli effetti della temperatura sulla nuova microbilancia per le analisi termo-gravimetriche nello spazio. Sono previsti gradienti di temperatura significativi sul cristallo a causa del riscaldatore incorporato il cui layout è vincolato dalla configurazione degli elettrodi; questo costringe a dissipazioni di potenze specifiche piuttosto elevate perché la potenza richiesta deve essere localizzata nella piccolissima area del film del riscaldatore. Come risultato, insieme alla temperatura (T) anche i gradienti termici (ΔT) devono essere compensati durante il TGA. L'accuratezza della misurazione della temperatura della QCM è importante perché è noto che la frequenza di oscillazione del cristallo dipende fortemente dalla sua temperatura. Una parte rilevante del lavoro è stata quindi dedicata alla taratura dei termometri QCM e alla valutazione della accuratezza di misurazione ottenibile.

La misurazione precisa della temperatura del cristallo ha permesso anche una determinazione accurata della relazione frequenza-temperatura. Il confronto tra le variazioni di frequenza in caso di temperatura uniforme e quelle osservate mentre si usano i riscaldatori sul cristallo ha dimostrato che i gradienti di temperatura hanno un forte effetto sulla frequenza.

Per identificare il campo di temperatura sulla superficie di un cristallo della QCM, è stata utilizzata l’elaborazione delle immagini termiche ed è stato sviluppato un modello termico. Il modello è stato inizialmente validato confrontando le temperature previste con quelle misurate attraverso la mappatura termica. Una volta validato, il modello termico è stato utilizzato per valutare i gradienti di temperatura su diversi cristalli e per diverse potenze in ingresso. Per correlare il gradiente di temperatura con la variazione di frequenza, è stata eseguita una campagna di prova con lo scopo di misurare le variazioni di frequenza derivanti da diversi livelli di potenza, generati sui riscaldatori del cristallo. In parallelo, le condizioni utilizzate durante l'attività sperimentale, sono state usate nelle analisi svolte col modello termico validato, valutando i gradienti di temperatura. Tramite questa campagna di test e analisi termiche è stato valutato l'effetto del gradiente termico. La frequenza si è visto essere accuratamente rappresentata con un polinomio di terzo ordine del gradiente termico medio. Infine, dopo aver caratterizzato sia l'effetto della temperatura media che del gradiente termico, è stata implementata una procedura di correzione degli effetti della temperatura. La validazione della procedura di correzione è stata effettuata con una nuova

campagna di test che ha evidenziato la presenza di errori residui inferiori al 7%. Pertanto il metodo di correzione sebbene migliorabile, con una campagna di prove più estesa e in condizioni di alto vuoto al fine di eliminare gli effetti di contaminazione, risulta promettente soprattutto per l'impiego della QCM ad alta temperatura nelle analisi termo-gravimetriche.

Parole chiave: QCM; gradiente termico; analisi termica; cristallo di quarzo; effetto piezoelettrico; stress termo-elastico; frequenza naturale; misura di massa; condensazione; TGA.

INDEX

FIGURE INDEX

TABLE INDEX

CHAPTER 1

1 QCM: INTRODUCTION

A quartz crystal microbalance (QCM) consists of a thin quartz disk with electrodes plated on it. The application of an external electrical potential to a piezoelectric material produces internal mechanical stress. The nature of the piezoelectric effect is related to the anisotropic behavior of the crystal. As the QCM is piezoelectric, an oscillating electric field applied across the device induces an acoustic wave that propagates through the crystal and meets minimum impedance when the thickness of the device is a multiple of a half wavelength of the acoustic wave. A QCM is a shear mode device in which the acoustic wave propagates in a direction perpendicular to the crystal surface. To make this happen, the quartz crystal plate must be cut to a specific orientation with respect to the crystal axes [1].

1.1 Materials

A piezoelectric quartz crystal resonator is a precisely cut slab from a natural or synthetic crystal of quartz. Quartz is namely a trigonal crystal that ideally has a crystal shape of a six-sided prism terminating with six-sided pyramids at each end. Natural mineral crystals are usually twinned (geminated) and many sub-crystals can grow up adjacently so that the original trigonal shape is hidden by the sharing/ cutting of some faces: thus, a natural quartz crystal shows a massive agglomerate. Anyhow, often quartz crystals are joined by one end to a common matrix and only the pyramidal other end termination is freed and shown.

Figure 1 A six-sided prism crystal and the natural quartz crystal as a massive agglomerate.

Two type of quartz structure are available: α-quartz and β-quartz. The first [2] is the most employed material for resonators and it is formed from silicon and oxygen. The transformation of one into the other form depends only on a mere rotation, without any structural change in crystalline links. The density of quartz is 2.65 g/cm^3, which is low, a result of its interatomic bonding. The mean refractive index of 1.55 is proportional to the

specific gravity. The material is chemically very stable because it is already fully oxidized. Because quartz is crystalline, it is electrically neutral since crystalline materials do not allow themselves to have a net electric charge. If any particular specimen has a high electrical conductivity, it is due to a large amount of interstitial cations. It is stable below about 573°C [3]. Quartz does not easily lend itself to fracturing along any particular plane or direction because the atoms are so closely bound together in all directions. When it does fracture, it has two tendencies: a shell-like curve appears on the broken surface called a conchoidal fracture; or a fracture will be parallel to one of the faces of the major or minor rhombohedron. Its crushing strength is 33 000 to 40 000 kg/cm^2. When the crushing strength is reached the crystal reduces to a fine powder. The tensile strength is about 1000 kg/cm^2 for small crystals. The tensile strength is slightly greater parallel to the optical, Z, axis when compared to the perpendicular. Twinning is common in quartz and can occur in various ways within a crystal. When twinning occurs, a twinning plane forms and the crystal begins to grow in a mirror image pattern relative to the original growth of the crystal. Twinning frequently results from inversion of a high-temperature, high-symmetry form to a low-temperature, low-symmetry form.

1.2 Anisotropic materials

Anisotropy is the dependence of a physical property on the direction. The quantities describing the mechanical behavior are generally not invariant, but depend on direction, precisely because of anisotropic behavior, and thus represent the response of the material to a very precise direction, not in an absolute sense. Quartz is a highly anisotropic material, i.e. some physical properties depend on the direction in which they are measured. The stress-strain behavior is described by a fourth order tensor. The Voigt notation is used to switch from tensors to matrix algebra and simplify the notation. Thus, the linear elastic behavior is described by a full 6x6 matrix and, considering that the latter should be symmetric, twenty-one coefficients are needed to fill it completely. In fact, the crystals manifest the behavior for which the mechanical response is directional but it is repeated in certain directions, due to the arrangement of the molecular constituents on a lattice arranged according to precise geometries. In the specific case of quartz, however, it is known that only six elastic coefficients are needed. This is the result of its trigonal lattice [4]. Hooke's law becomes the following:

$$\sigma = \begin{bmatrix} C_{11} & C_{12} & C_{13} & C_{14} & 0 & 0 \\ C_{12} & C_{11} & C_{13} & -C_{14} & 0 & 0 \\ C_{13} & C_{13} & C_{33} & 0 & 0 & 0 \\ C_{14} & -C_{14} & 0 & C_{44} & 0 & 0 \\ 0 & 0 & 0 & 0 & C_{44} & C_{14} \\ 0 & 0 & 0 & 0 & C_{14} & C_{66} \end{bmatrix} \varepsilon \tag{1.1}$$

The values can be found in literature [5]. Notice also that among the six coefficients, only five are independent:

$$C_{66} = \frac{1}{2}(C_{11} - C_{12}) \tag{1.2}$$

The coefficients found in literature are referred to the optical axis (X and Y). They are not perpendicular to the quartz crystal disk (AT cut). In order to switch to a local coordinate system where Z' and Y' are perpendicular to the disk, a base rotation of (90°- 35.25°) along X was performed as reported in the Raddani thesis, ANNEX A [6].

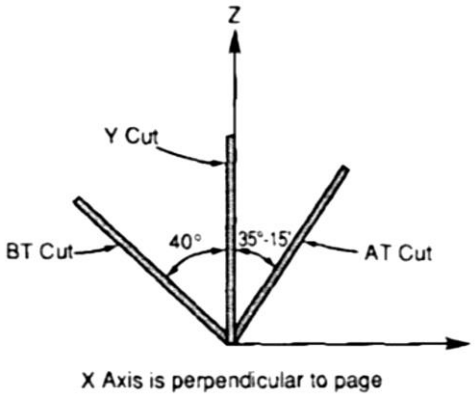

Figure 2 Cut planes for quartz crystals with respect to the X-Y-Z axes.

1.3 Piezoelectric effects

Piezoelectricity is the capability of some crystalline materials to electrically polarize as a consequence of a natural elastic mechanical deformation (direct piezoelectric effect), and vice versa, to deform elastically if subjected to the action of an electric field (inverse piezoelectric effect, or Lippmann effect) [7]. So, piezoelectric bodies show an electric charge if subjected to a mechanical stress (direct effect) or vice versa they deform if in presence of an electric field (inverse effect). The behavior is explained by a microscopic cause: electrical dipoles internal to the piezoelectric material induce the opposite charging on the opposite side of the crystal; the product of the opposite charges' amounts gives the charge momentum at any side of the dipole times the distance gap beneath them. The following equation shows how relates mechanical and electrical parameters:

$$\Delta L = E d L_0 \tag{1.3}$$

where L_0 (m) represents the initial height of the crystal, ΔL (m) its compression, E (V/m) the electric field intensity and d (m/V) the coefficient of piezoelectricity of the ceramic. Being $\Delta L/L$ the axial strain, the formula highlight that strain is proportional to the electric field applied.

Piezoelectricity is a phenomenon of the crystalline state, and these materials are anisotropic (i.e., dependent on the axial direction) in many properties. In addition, crystals that exhibit this property are dielectric, electrically non-conducting. Quartz is an excellent insulator, or dielectric, except at high temperatures. A necessary condition for piezoelectricity is that the crystal lacks a center of symmetry. Quartz meets these criteria.

1.4 QCM: theory and operating principle

The working principle of the Quartz Crystal Microbalance (QCM) is based on the piezoelectric property of the quartz. The theoretical foundation of piezoelectricity was first investigated by Jacques and Pierre Curie in 1880 [8]. Piezoelectricity is the primary property of the crystal, which make it usable as a resonator. Piezoelectricity is defined as 'the electric polarization produced by mechanical strain in crystals belonging to certain classes, the polarization being proportional to the strain and changing sign with it.' This polarization can be produced by strain such as, shear, tension and compression on a piece of quartz. The nature of the piezoelectric effect is related to the anisotropic behavior of the crystal. A force that deforms the lattice causes a net movement of positive and negative charges, which results in the manifestation of the electric dipole moment. Due to this center of gravity, a voltage appears and this does not happen if the crystal has a perfectly isotropic lattice. Piezoelectricity happen also when quartz interacts with an oscillating electric field. The application of an external electrical potential to a piezoelectric material produces internal mechanical strain. Therefore, an oscillating electric field applied across the device induces an acoustic wave that propagates through the crystal, in accordance to the properties that the latter meets the minimum impedance when the thickness of the device is multiple of the half of its wavelength. The QCM is a thickness shear mode (TSM) device in which the elastic wave propagates in a direction perpendicular to the crystal surface. Pure thickness shear vibrations happen when the top and bottom surfaces slide parallel to each other for the same distance but opposite direction. This causes the midplane not to move at all and the lateral surface to deform in a shape. Since quartz crystals show different modes of vibration depending on the orientation of the lattice, a precisely cut disk from a slab should be used in order to guarantee that thickness shear mode is possible.

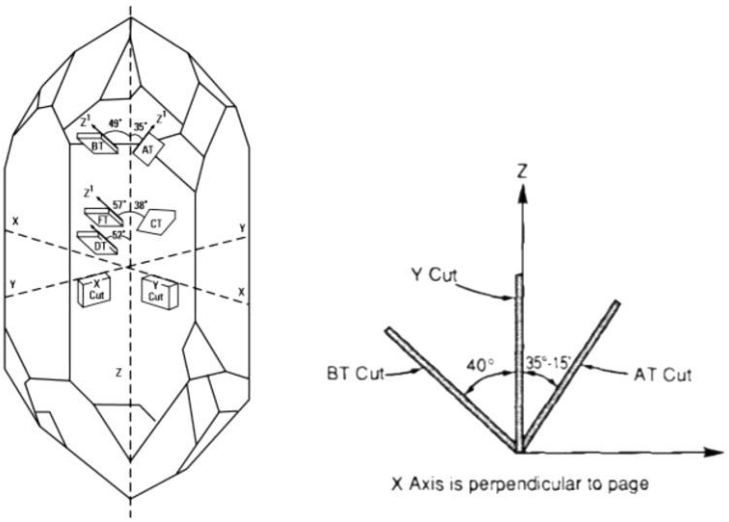

Figure 3 Typical cut planes for quartz crystals.

The AT cut is the most common choice for microbalance applications. TSM is possible in an AT-cut quartz disk. The modal frequency can be analytically predicted. It was previously anticipated that the elastic waves tend to appear spontaneously when the thickness of the device is a multiple of a half of its wavelength. A simple consideration on the measurement units leads to the following equation.

$$f_n = \frac{v}{2h} \tag{1.4}$$

where v is the velocity of elastic wave and h is the thickness of the crystal.
It is also known from the theory of modal analysis that:

$$v = \sqrt{\frac{C_{ij}}{\rho}} \tag{1.5}$$

where ρ is the density and C_{ij} is the elastic modulus associated with the elastic wave being propagated. By combining Eq. 1.4 and 1.5, it follows that:

$$f_n = \frac{1}{2h}\sqrt{\frac{C_{ij}}{\rho}} \tag{1.6}$$

that is a simple expression for the vibration natural frequency. It is clear that the proper shear modulus must be used in order to study the TSM of quartz plates. TSM happens also at odd multiples of f_n. These modes are called overtones and they are exploited when a high frequency resonator is needed. In the QCM, the electrodes provide the contact necessary for inserting the device in an electrical circuit aimed at providing the electric excitation field. Moreover, they make the resonator thicker at the center than at the rim. The idea behind this design choice is to use the energy trapping effect to confine the displacement field in the center and make it small at the edges. This ensures low losses or, equivalently, a high Q factor, which is the ratio of frequency and bandwidth [9].
A QCM exploits the thickness shear mode for detecting mass changes. Sauerbrey showed that a small mass deposit causes a decrease in the initial resonant frequency according to the following equation [10]:

$$\Delta f_n = -\Delta M \frac{2f_n^2}{A\sqrt{G\rho_q}} \tag{1.7}$$

where Δf_n is the resonance shift, ΔM is the deposited mass change and f_n is the unloaded natural frequency. A, G, ρ_q are parameters describing the microbalance: respectively the electrode area, the quartz torsional modulus of elasticity and the density. The equation was obtained under the hypothesis that the mass deposited on the microbalance is a circular quartz disk with same area of the electrodes. Equation 1.5 is also referred to as mass loading effect. It is valid for frequency shifts smaller than 2% of the initial resonance. After this limit, the equation becomes non-linear and corrections must be introduced [11]. The equation shows also that high initial natural frequencies lead to higher mass sensitivity. More specifically, a properly designed QCM can detect changes in surface mass density of roughly one ng/cm^2 provided that it is possible to accurately sense frequency shifts of a few Hz [12].

Many design factors influence the resonant condition of the device. Specifically, the most important one is the thickness, followed by the cut, size, shape and quality of the crystal [13]. In addition, the presence of the electrodes must be taken into account. Because of these many variables, spurious modes occur [14]. This is shown in the example of a quartz disk's frequency response function:

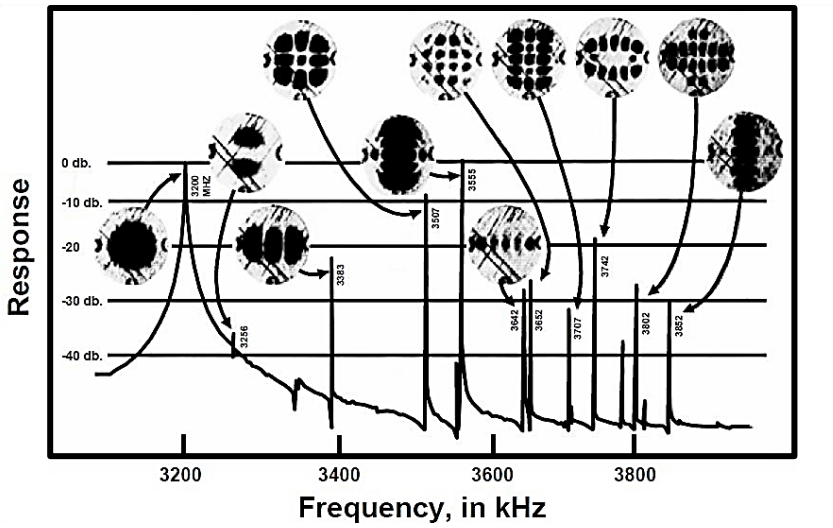

Figure 4 X-ray topography of various mode excited during the frequency scan of a fundamental modes, circular, AT-cut resonator.

The first peak denotes the principal TSM. This conclusion can be drawn by looking at the deformation shape, which is uniform (the entire disk is dark colored). Aim of a correct design is to work at that specific frequency (3.2 MHz in the example). The other visible peaks indicate the presence spurious modes. They are in general not critical since they take place at frequencies sufficiently far from the main one so that coupling with the TSM does not happen. Nonharmonic overtones, on the other hand, are undesirable as they may lead to the generation of unwanted signal corruption, thus decreasing the accuracy of the measure. They are visible in the small wavy parts of the response curve. Strict design rules are used to minimize these unwanted modes.

The frequency detection is critical when operating a QCM. Many factors influence the frequency stability of a resonator.

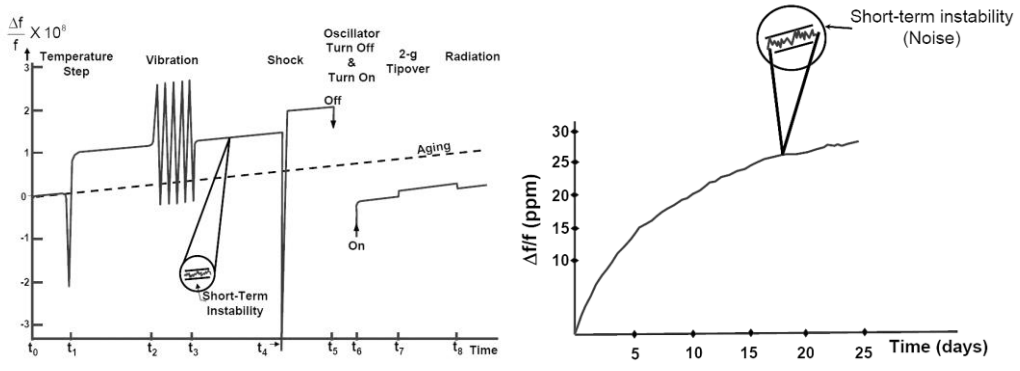

Figure 5 Major types of oscillator frequency instabilities on the left. Aging and short time instability on the right.

Considering the major oscillator instabilities, a step in the working temperature or a thermal shock can cause instantaneous instabilities. On the other hand, aging, short-term instabilities and thermal fluctuations are time dependent phenomena. Aging, according to the definition internationally adopted, is a systematic change in frequency with time [15]. The main causes of aging appear to be mass transfer to or from the resonator surfaces (due to adsorption and desorption of contamination) and stress relief within the mounting structure or at the interface between the quartz and the electrodes [16]. Therefore, in order to achieve low-aging, crystal units must be fabricated and hermetically sealed in ultraclean, ultrahigh vacuum environments. Short-term instabilities are essentially synonymous of noise. Temperature fluctuations, random vibrations, thermally induced charge fluctuations (Johnson noise) and electrical circuit defects are all possible causes. Thermal loads, hysteresis [17] and thermal shocks also affect the frequency-temperature-time response of the QCM [18].

A stress field is another important source of frequency changes. There are varieties of stresses built, inadvertently, into a newly manufactured resonator. They might be caused by thermal expansion coefficient local differences, residual strains in the quartz or in the electrodes, mounting or bonding operations [17]. Accelerations (gravity, shock, and vibrations) [19], iodizing radiation [20], atmospheric pressure and humidity have to be considered, among the other factors, with particular attention in some specific applications [21].

1.5 The developed QCM device with criticalities and applications

Differently from other mass sensors, QCMs can operate in micro or zero gravity environments as their oscillation generates a very strong acceleration field. This characteristic, coupled to their low mass and volume, makes them particularly well suited for space applications. In addition, it also gives them sensitivities much higher than those of the other mass sensors commonly used in laboratory, even reaching a mass detection threshold of few ng per cm^2. So, QCMs are often used in thermo-gravimetric analysis (TGA), a widely established technique to investigate deposition/sublimation and absorption/desorption processes of volatile compounds in different research areas, such as outgassing contamination in space, dehydration and organic decomposition in minerals, moisture content in foods and the development of temperature profiles for firing ceramics. In particular, the possibility of its use for dust deposition monitoring, measurement of mass deposition for small size particles in cleanliness sensitive sites or celestial bodies surfaces, has been considered. When the sample is heated, its most volatile component desorbs or sublimates; this allows measuring the mass of the volatile component (obtained as difference between mass before and after the desorption process respectively) and its composition (inferred by desorption temperature). Changes of the sample mass causes QCM resonance variation that is computed through the Sauerbrey relation.

The main component of the QCM device object of this work consists of an oscillating quartz crystal with an integrated micro-heater that can be extremely useful in the study of desorption of volatile compounds from refractory materials. The concept is the subject of a

patent (1987) but it has not been implemented in a device [22]. The innovation behind the proposed concept is actually the deposition over the crystal of film resistors exploited both as heater and temperature sensors for TGA. The quartz crystal plate with two electrodes and two resistors deposited on the top and bottom surfaces to measure the shear resonance of the crystal, represent the adopted configuration. This allows direct temperature measurement over the sensing area, useful because the oscillating frequency of the crystal depends on its temperature. In literature, the effect of the temperature on the thickness shear mode device has been considered only in case of uniform distribution. The microbalance under study conversely, operates under a non-uniform thermal field when heated. This fact is a consequence of its innovative heater design, which provides power to the adjacent electrode area by conduction. This condition must be studied because unexpected frequency shifts have been observed during the high power phases required to induce fast temperature changes. The major result found was that the frequency at which the device vibrates was significantly higher than observed in the uniform temperature distribution case (the majority of the devices are heated through their envelope). The obtained results so far suggest that it might be necessary correcting this shift when operating the microbalance in practice; nevertheless, first of all it is needed to understand how this frequency shift is generated and how it can be modeled or described.

The final goal is the development of a microbalance that can be operated in a wide temperature range, under variable environmental conditions in terms of temperature and radiative fluxes and able to perform TGA at high temperature, measuring both condensate and solid particles. The characterization and modelling of the temperature effects on the quartz crystals is seen as the major step to achieve the final goal. In literature, the temperature dependence of the crystal's resonance frequency has been extensively analyzed nevertheless, the effect of temperature gradients over the crystal surface has been neglected. The localized heating in restricted areas of the crystal however, generates stronger temperature gradients therefore, the effect of gradients negligible in the legacy configurations is likely to become significant. As result, along with the temperature (T) also the thermal gradients (ΔT) will have to be compensated during TGA.

1.6 Scope of the thesis

The last experimental activities on the microbalance have shown that the thickness shear frequency at ambient temperature is correctly found at 10 MHz. Moreover, uniform temperature distribution has been applied to the crystal in order to evaluate the temperature-frequency relationship. Subsequently a temperature gradient has been applied and it was observed a resonance shift, highlighting the importance of the temperature gradient on the microbalance. In fact, the microbalance's innovative heater causes thermal gradients that, although not critical from the point of view of mechanical resistance, causes frequency shifts. In the current literature, the effects of thermal gradients on the frequency-temperature curve have not been addressed in detail. This is mainly because most of these kind of devices works at uniform temperature.

Previous studies always identified conditions in which thermal fluctuations happen as not usable for QCM, this was identified for instance for solid polymer film coated QCM. The problem becomes significant in applications where the sensors operates in dynamically

variable environment over wide temperature range or with varying external heat fluxes e.g. because of sun illumination. Compensation of the (uniform) temperature effects in microbalances is therefore still an issue. The problem is complex because many parameters affect the frequency sensitivity mainly crystal angle cut and thickness but, even small variation in the crystal electrodes thickness cause thermal sensitivity variations due to the different mass loading on the surface. In such situations, the sensors readings will be superimposed with the QCM's temperature induced frequency shifts and this will cause measurement errors. In order to compensate the temperature effect, a viable solution would be based on a dual mode SC-cut QCM. Such a system allows in principle efficient separation of the thermal effects from the sensor response. Nevertheless, this solution has been dropped due to the difficulty and cost of manufacture. The most common solution, uses a dual QCM oscillator in which the first quartz crystal is used as reference device, while the other one is the sensor. To minimize thermal gradients, both channels could be fabricated on the same quartz substrate that nevertheless is a poor thermal conductor therefore not granting a uniform temperature, so the usage of separated crystals is more common. In this configuration, the sensor signal is obtained from the beat frequency between the two resonators, assuming that the temperature variation will cause equal frequency shifts for both devices. Unfortunately, it is difficult to fabricate two coated QCMs with exactly the same temperature sensitivity because of the tolerances in the metallization parameters and the thickness of the sensitive coating from device to device, will introduce different temperature behavior of each crystal as observed with Rayleigh surface acoustic wave (SAW) devices. This again causes measurement errors over the thermal operating range. Therefore, also this solution has been abandoned in many cases and a single crystal coated at a certain polymer thickness has been investigated.

The research aims first of all at optimizing the performances of the microbalance and it will be carried-out following the classical approach. The behavior of the current model of microbalance will be characterized in terms of sensitivity to environmental temperature and radiative fluxes, simulating the operative conditions in space under variable sun illumination. The issue of the sensitivity to temperature gradients will be carried-out in parallel with the design of an experimental campaign allowing to characterize the quartz crystal behavior under different temperature distributions and finally the implementation of the models of the quartz crystal resonance frequency for the compensation of the identified input disturbances.

Another activity has been performed with respect to the sensitivity of the microbalance to dust deposition. Despite the problem is relevant for the QCM application, it is not related to the temperature effects which is the main goal of our study. Therefore the analysis has been inserted as annex (Annex C). The analysis did not give definitive results but showed however that the microbalance cannot be used to measure powders deposition of non-controlled granulometry.

CHAPTER 2

2 THE UNIFORM TEMPERATURE EFFECTS ON THE FREQUENCY VARIATIONS

Differently from other mass sensors [23], QCMs (Quartz Crystal Microbalances) can operate in micro or zero gravity environments as their oscillation generates the acceleration field on which the mass measurement rely. This characteristic, coupled to their lightness and size, makes QCMs potentially well suited for space applications. The core of the instrument consists of an oscillating quartz crystal with an integrated micro-heater that can be used to regenerate the crystal once deposited mass leads to saturation or can be used to generate the desorption of volatile compounds from refractory materials by heating or to perform TGA. The quartz crystal plate comprises two electrodes and two film resistors deposited on the top and bottom surfaces to measure the shear resonance of the crystal, along with its temperature and at last allowing the direct delivery on it of heat for thermal control [24, 25]. The accuracy of the temperature measurement of the QCM is crucial because the oscillating frequency of the crystal strongly depends on its temperature [26]. Actually, in most laboratory applications, the environmental temperature is controlled within few degrees Celsius and the correction of the measured frequency is generally not even required. Unfortunately, this is often not possible for microbalances to be used in Space, where the environmental temperature control is difficult or sometimes even not possible, and radiative fluxes can strongly affect the crystal temperature e.g. in case of sun illumination. The localized heating in restricted areas of the crystal however, generates stronger temperature gradients therefore the effect of gradients negligible in the legacy configurations is likely to become significant. As result, along with the temperature (T) also the thermal gradients (ΔT) will have be compensated during TGA. Previous studies on this effect are not available; therefore, its investigation is one of the goals of this study. First of all, the calibration of the QCM thermometers within the expected working temperature range is essential to allow for the correction of the temperature effect on measured data which is paramount important especially in space application where the expected temperature range is very large. Moreover it is a key information once TGA measurements are performed.

2.1 Calibration of the QCM deposited temperature sensors inside the thermal bath

2.1.1 Setup description and tests

Calibration of the embedded temperature sensors has been performed in order to determine the temperature- electrical resistance relationship for the deposited films (deposited materials are 140 nm and 40 nm of chromium and gold, respectively). In order to assess measurement reproducibility, four different crystals have been tested, i.e. QCM 1, QCM 2, QCM 3 and QCM 4, characterized by nominal natural frequency of 10 MHz and

circular shape, with diameter and thickness of 13.95 mm and 0.167 mm, respectively. The quartz crystals have been tested between -20°C and 100°C inside a thermal bath, providing uniform temperature environment. Each crystal has been mounted on a mechanical support designed to provide a compliant mounting to avoid thermal stresses in a wide temperature range. View of the setup for the calibration of the deposited thermometer is provided in Figure 6.

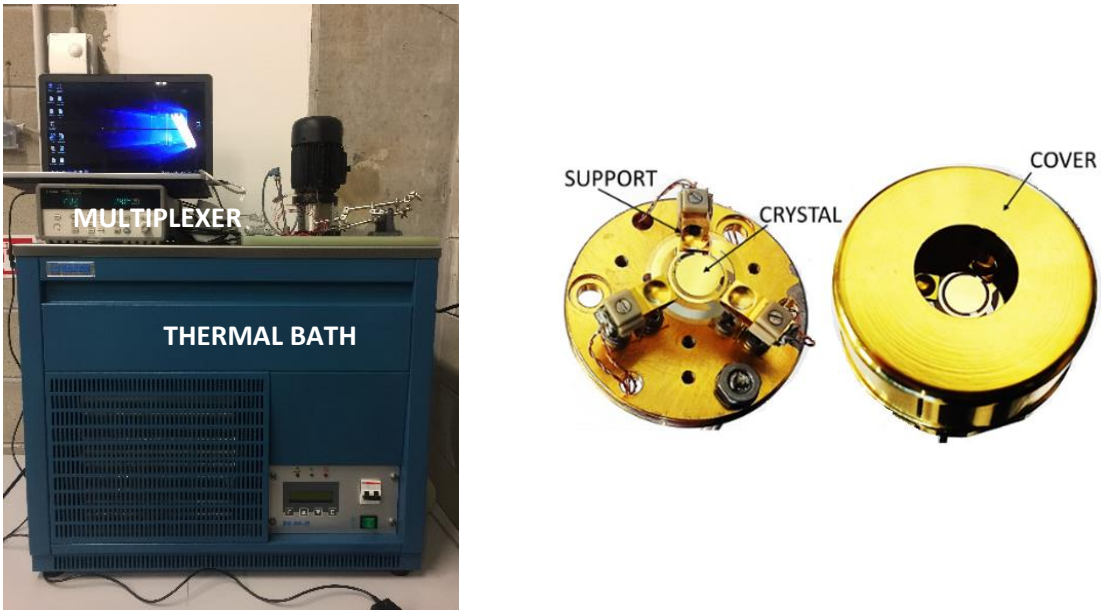

Figure 6 QCM testing setup: (right) detailed view of the crystal mounting structure, (left) overall view of the measurement chain

The mechanical support has been placed inside the thermal bath (filled with silicon oil). The thermal bath warrants a horizontal temperature uniformity of ± 0.01 °C between 35°C and 80 °C and the vertical uniformity of ±0.012 °C at 35°C and ±0.006 °C at 80 °C. To perform the calibration, the temperature inside the thermal bath has been measured with a platinum resistance sensor PT100, while the Electrical resistance of the deposited films have been measured by means of a multiplexing unit Agilent 34970A with a 4 wires measuring circuit.

2.1.2 Results and discussion

Results of the thermal cycles (ramping up and down) are displayed in Figure 7. Table 1 summarizes the linear regression results and the expected temperature measurement uncertainty.

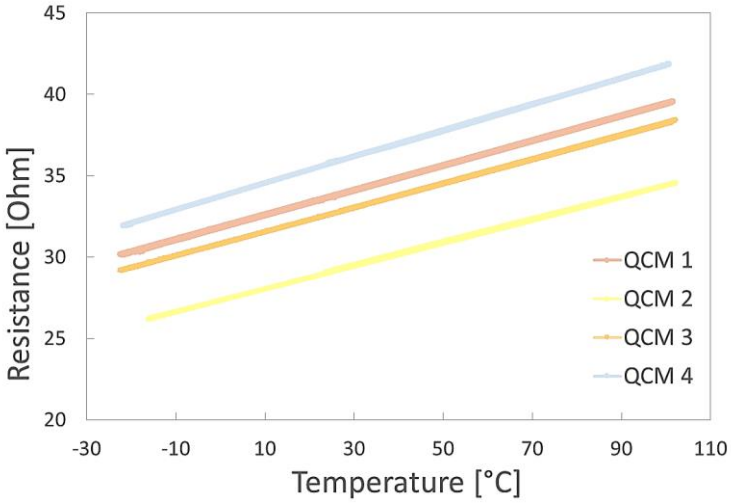

Figure 7 QCMs calibration results: measured electrical resistance and temperature layouts.

Table 1 Linear regression and standard deviation results.

QCM	S [Ω/°C]	R_0 [Ω]	Linearity standard deviation [Ω]
1	0.076	31.80	0.0042
2	0.069	27.46	0.0111
3	0.074	30.84	0.0025
4	0.081	33.73	0.0280

Experimental results evidenced high linearity of the deposited thermometer, leading to an instrumental uncertainty of about 0.2°C using the linear model within investigated temperature range. The uncertainty, computed dividing the linear standard deviation [Ω] by the sensitivity [Ω/°C], of the QCM 4 is equal to 0.3 °C, slightly higher with respect to the other crystal. That is due to modified characteristics of the crystal that will be used for the thermal gradient analysis (described in the chapter 3). Despite of a polynomial regression having less uncertainty, the linear one is sufficient for the TGA analysis and to measure the temperature of the crystal for the intended application.

2.2 Uniform temperature-frequency relationship inside the Thermal Bath

Once calibrated the temperature sensors, the effect of different uniform temperatures of the crystal on its resonance frequency has been determined.

2.2.1 Thermal Bath testing setup

QCM1 has been selected for the determination of the oscillating frequency vs temperature relationship. Testing has been initially performed using the thermal bath between -20°C and 100 °C, similarly to what was done for the calibration of the embedded thermometers. To avoid the effect of the fluid on the resonance frequency the QCM cannot be just immersed in the thermal bath as was done for the thermometers calibration. A setup with a sealed

aluminum enclosure has been designed in order to test the crystals. This was necessary to avoid the direct contact of the QCM with the fluid that would prevent the resonance measurements. In Figure 8, a scheme of the measurement setup is reported.

The temperature of the bath has been changed with ramps at 0.5 °C/min slope; three cycles have been performed to verify measurement repeatability. The Agilent 34970A multiplexing unit has been used to acquire the deposited resistance and the frequency counter VICTOR VC3165 (Resolution 10 Hz) to measure the frequency.

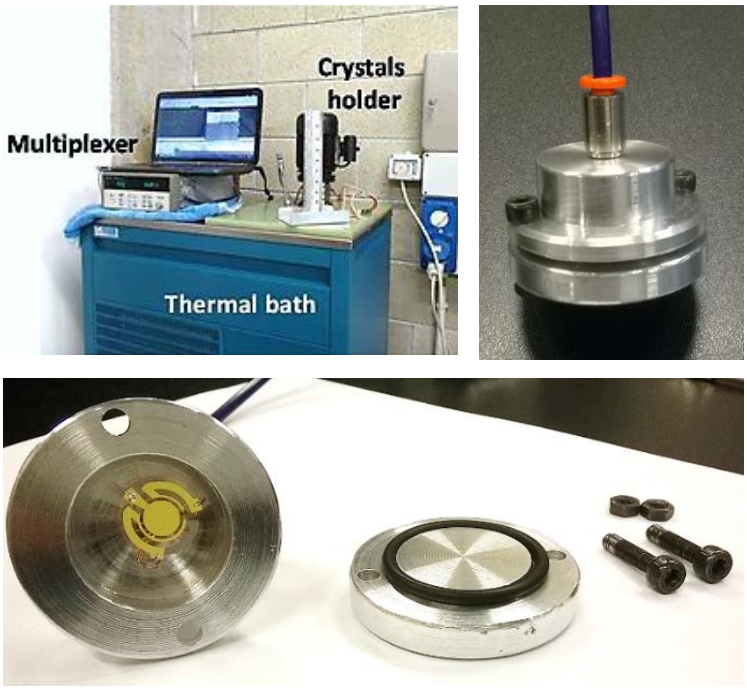

Figure 8 View of the measurement setup with QCM1 and sealing element.

2.2.2 Thermal Bath testing results

Measured trend has been compared with theoretical behavior (AT-cut quartz crystal with ϑ equal to 35° 15') found in literature [5]. Measured values are plotted in Figure 9 along with the model and one can notice that they exhibit the same trend i.e. that of a third order polynomial but differences are evident.

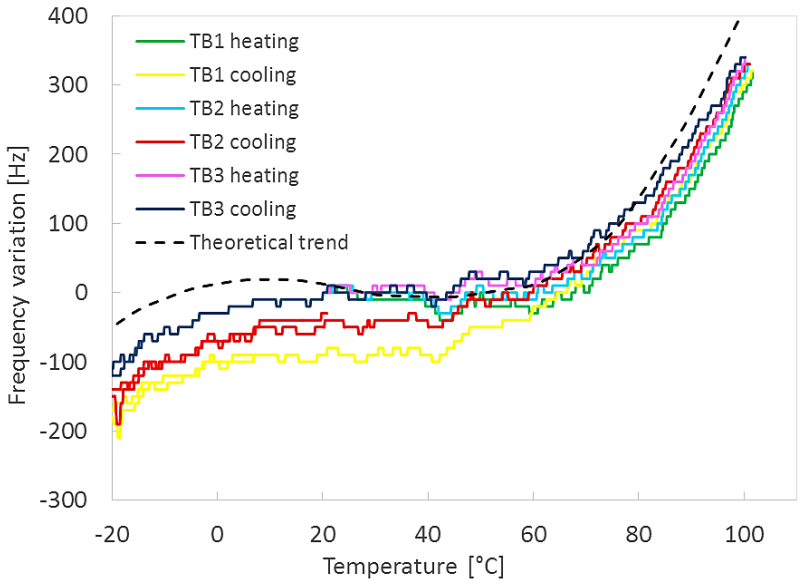

Figure 9 Frequency variation vs temperature for the QCM 1 in the thermal bath.

Beside the differences with the model that can be justified by the actual characteristics of the crystal, the test results evidence that coming back to ambient temperature after the heating at 100°C leads to frequency changes. In particular, the temperature cycles provide a negative shift with respect to the theoretical trend of about 100 Hz at 0°C. The repeatability standard deviation, on the three cycles, has been computed at 24.2 Hz.

These results have been explained with contamination phenomena occurring within the cryostat, mostly at high temperature. Quite likely, the oil smearing the sealing, the epoxy glue or the electrical wires plastic insulation when heated release some low boiling temperature organics that migrates inside the cryostat and can condensate on the crystal that at least during heating is the coldest surface. Furthermore, it has been observed that the largest frequency drop is achieved after the first heating cycle while cooling cycles tend to rise from cycle 1 to cycle 3. This leads to assume that the system has been stabilizing during the sequence of the cycles and the crystal partially cleaning. To verify the hypothesis of crystal contaminations, the deposited heater has been exploited to clean it. The crystal has been heated until the temperature of 100°C has been reached for few minutes. After the heating cycle, the frequency returned to the initial value, as shown in Figure 10. It can be noticed that in the case without the heater on, the contamination occurs and that is evidenced by the negative shift of the blue curve, that represent the uniform temperature heating, with respect to the light blue curve that represent the uniform temperature cooling. Once the heater is switched on, the heating (yellow curve) and the cooling (green curve) are almost coincident. This result means that the crystal has kept clean once the heater has been turned on so, no shift is present at ambient temperature after the cycle has been completed.

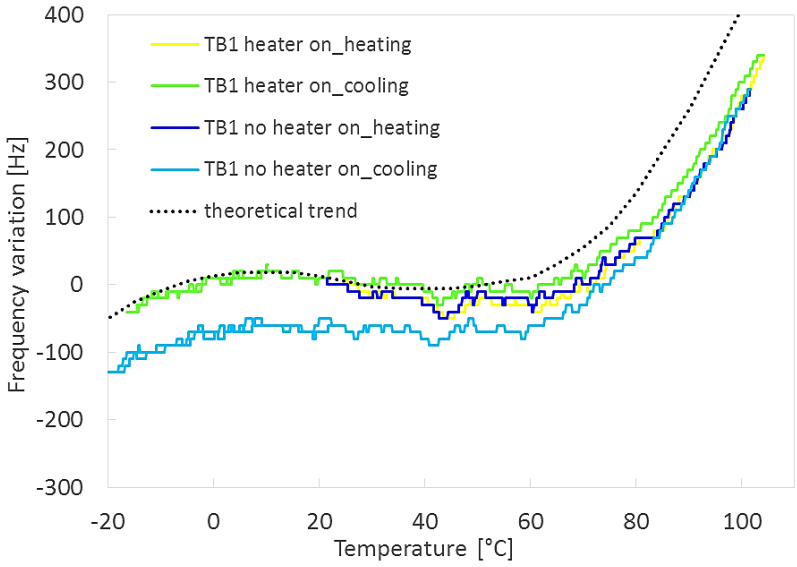

Figure 10 Frequency variation vs temperature considering the deposited heater on the QCM 1 after "regeneration" at high temperature.

Despite the contamination effect was proved by this test the visual inspection of the system did not evidence smearing of the crystal or of the enclosure internal surfaces, proving that there was no "sealing failure" but just the cleanliness achievable was insufficient. This result eventually induced to discard this kind of setup and to look for a cleaner environment.

2.3 Uniform temperature-frequency relationship inside the Vacuum chamber

Contamination issues found with the thermal bath testing, led to place the measurement setup inside a vacuum chamber in order to guarantee a cleaner environment, avoiding the trapping of degassing products within the microbalance enclosure; outgassing probably would occur but volatiles should be mostly removed by the vacuum pumping system.

2.3.1 Vacuum Chamber testing setup

The test on the crystal has been performed between 20°C and 100 °C with an internal pressure of 0.1 mbar (measurement uncertainty of ±15% of the reading), granted by a rotary vacuum pump Varian DS 402. In order to provide heating and cooling of the crystal, the cryostat has been mounted over a thermoelectric cooling element, a platinum temperature sensor monitored the TEC temperature during the test. A water cooling circuit was used when the TEC heatsink cooling was required. The crystal temperature has been measured by means of the embedded sensor. View of the measurement setup is shown in Figure 11.

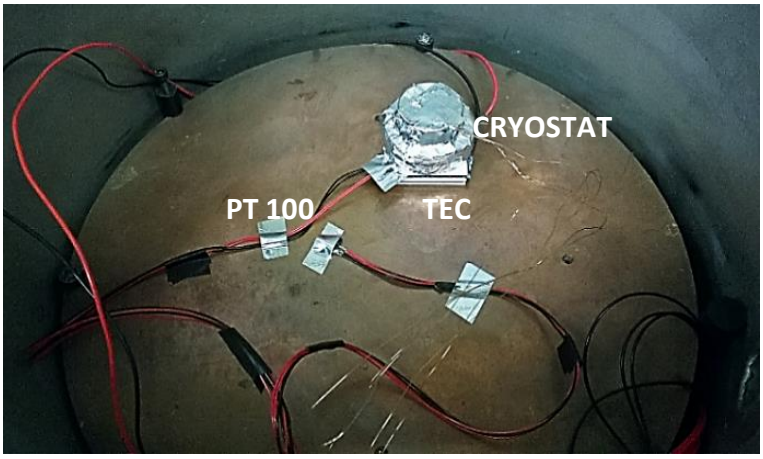

Figure 11 Vacuum testing measurement setup.

Three cycles have been performed within investigated temperature range, as shown in Figure 12. The TEC has been used in reverse mode during heating and in normal mode when cooling was required.

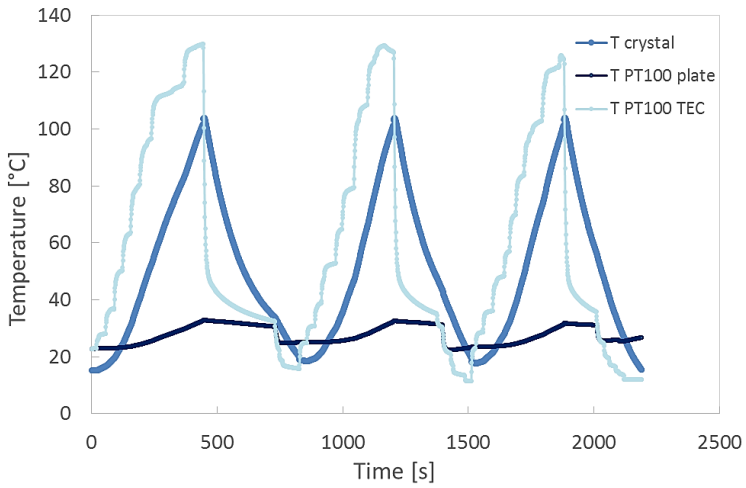

Figure 12 Three cycles for temperature and resistance.

2.3.2 Vacuum Chamber testing results

Measured frequency variation vs temperature in vacuum testing is shown in Figure 13. The three cycles have been analyzed and 12.6 Hz repeatability standard deviation has been computed. Comparing the repeatability of the thermal bath tests with those of the Vacuum Chamber, one can see that a reduction by a factor two has been achieved.

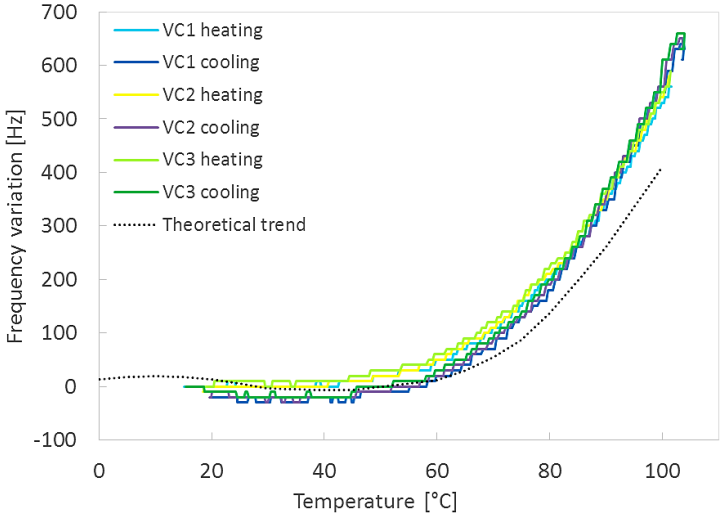

Figure 13 Frequency variation vs temperature for the QCM 1 in the Vacuum Chamber

Nevertheless, analyzing in detail the measured trends, it can be shown that the measured frequency variation is still characterized by a negative drift of the frequency curves among the cycles, evidencing that some contamination is still occurring. Despite the small contamination, a third order polynomial model has been obtained (Figure 14): the regression standard deviation is 13 Hz. The regression standard deviation evaluated on the single cycle or on the three cycles is the same proving that the process is repeatable. The correction accuracy in the considered temperature range is less than 2% of the full scale effects, which is acceptable for the time being; therefore, the goal of frequency-temperature characterization was considered achieved.

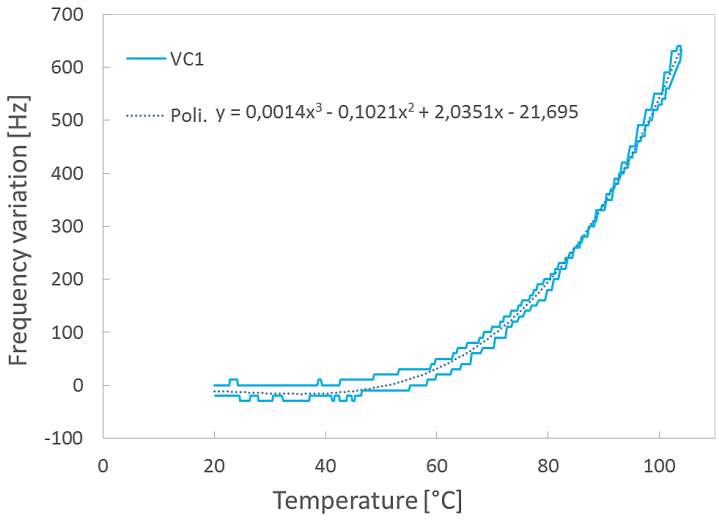

Figure 14 Polynomial regression of the heating and the cooling cycle VC1.

Operating in high vacuum would be advisable; this improvement is planned for a next test campaign in which also the resolution of the frequency measurement system (10 Hz in this setup) will be reduced to 0.1 Hz with an improved frequency-counter. The instrument has proved to be very sensitive to contaminating environment; on one side, this justifies that it

is of primary interest to accurately measure and monitor contamination in Space but, on the other hand, this leads to a tough challenge for its temperature effects calibration, especially with high temperatures that promotes materials outgassing.

2.3.3 Miniature Vacuum Chamber uniform temperature-frequency relationship for the crystal used for the thermal gradient identification

A uniform temperature distribution effect has been tested for the crystal QCM 4: this is a special specimen that underwent on one side the gold coating removal in order to allow the temperature mapping through IR camera as will be described in detail in the next chapter. An updated setup, to perform the uniform temperature test, has been designed to guarantee a clean environment and a uniform temperature distribution.

A small cryostat has been designed and manufactured with two small chambers, one to hold the crystal, the other to allow the cables to escape in order to acquire the data: the deposited resistance to determine the crystal temperature acquired using the Agilent 34970A multiplexing unit and the frequency collected with the frequency counter Agilent Keysight 53220A 350 MHz (resolution 0.1 Hz). The cryostat has been aimed to maintain the vacuum generated by the rotary pump Varian DS 402: two rings have been used, one placed between the two chambers and another between the cryostat and the pump tube. The setup has been placed inside a climatic chamber Angelatoni Challenge 250 warranting a uniform temperature distribution in the range between 0 to 100°C with a maximum gradient of 2 °C/ min. In the following, the view of the testing setup has been displayed in the Figure 15:

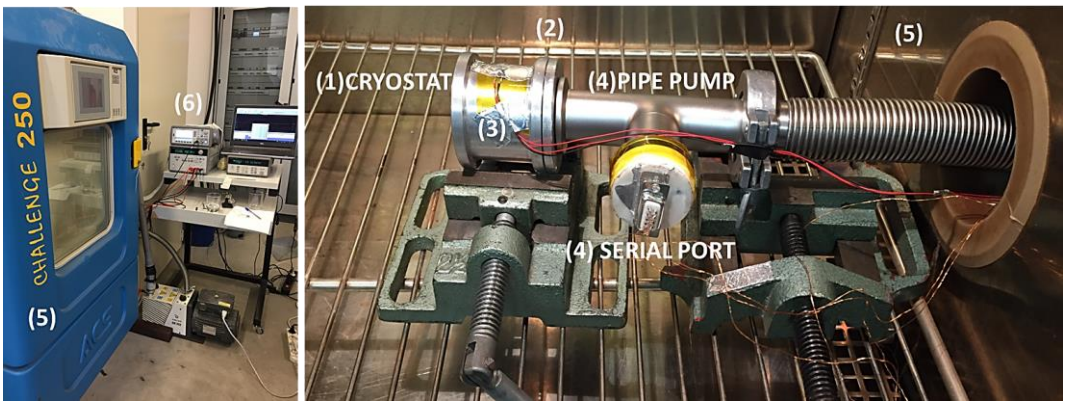

(1)	CRYOSTAT
(2)	O-RINGS
(3)	PT100 TEMPERATURE SENSOR
(4)	SERIAL PORT
(5)	CLIMATIC CHAMBER
(6)	ACQUISITION DEVICES

Figure 15 Setup for the testing uniform temperature-frequency relationship

Measured frequency variation vs temperature is shown in Figure 16. The cycle has been analyzed and a third order polynomial model has been obtained. The computed regression standard deviation is 12.25 Hz.

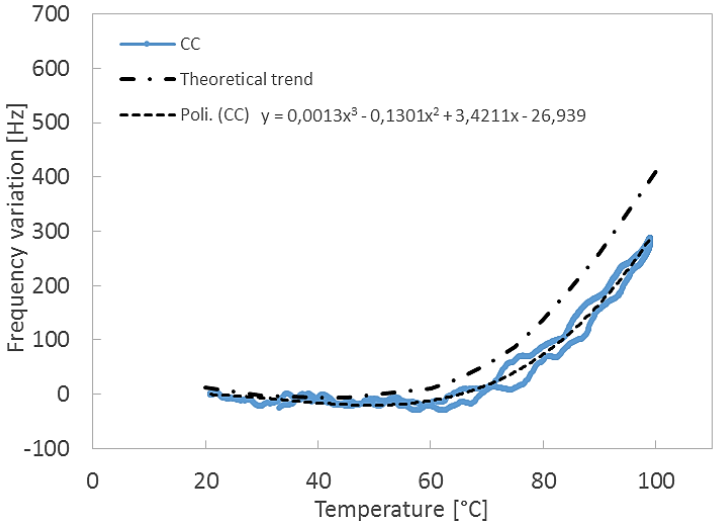

Figure 16 Polynomial regressions of the heating and the cooling cycles.

The lower frequency variation with respect to the theoretical trend is not expected, but the crystal used is the one with the removed gold ('modified'). The procedure is limited by the fact that a modified crystal is used and therefore this difference has not been further investigated. Moreover, the vacuum in the chamber is not high and therefore contamination cannot be excluded though there is no residual shift at room temperature.

2.4 Conclusions

In these tests, a special care has been made to impose a uniform temperature over the crystal. This work provides the temperature-frequency characterization of a quartz crystal microbalance for thermogravimetric analyses in space. The analyzed microbalance comprises innovative built-in heater and temperature sensor. This gave the chance of measuring the crystal temperature of the sensing area with minimum insertion error, and right on the electrode border allowing to perform the calibration of the oscillating frequency vs temperature. Crystal calibration has been performed within a temperature-controlled enclosure and in vacuum. Qualitative agreement with the literature models has been evidenced, complete matching is not expected because of the dependency on the crystal lot manufacturing characteristics. Repeatability issues led to highlight the sensitivity of the instrument to the contamination that was significant even in medium vacuum environment (0.1 mbar).

CHAPTER 3

3 DETERMINATION OF THE THERMAL FIELD ON THE CRYSTAL

The effects of temperature on a TSM device have been discussed from a wide perspective. However, the previous chapter deals with a uniform temperature distribution. As for the microbalance under study, it is known that it operates under a non-uniform thermal field when heated. This fact is a consequence of its innovative heater design, which provides power to the adjacent crystal areas by conduction. For this reason, understanding the effect of a non-uniform thermal field on the microbalance is necessary in order to correct the measured data.

3.1 Experimental determination of the temperature field

The purpose of this activity is to identify the temperature distribution on the crystal surface by using an infrared camera. However, the thermal imaging introduces some problems such as:

- The infrared camera accuracy: the camera has a quite high uncertainty from manufacturer specifications. This is normal because, in common measurements, this uncertainty becomes negligible with respect to the contributions deriving from surface emissivity. Nevertheless, in our procedure the emissivity is measured using thermal camera too therefore, its accuracy becomes crucial. The camera thermal calibration, by using a black body has been performed to reduce the uncertainty applying a “corrective factor” temperature dependent. This latter ‘Fc’ is used to determine the emissivity on the different crystal materials and afterwards the temperatures of the different parts.
- The emissivity determination: to allow the image processing, even with the (low emissivity) gold film removed, an accurate knowledge of the emissivities is required; the emissivities were therefore preliminarily measured.

3.1.1 Calibration of the infrared camera

To reduce the infrared camera instrumental uncertainty it has been calibrated by using the black body DIAS CS 110. The black body, available in the laboratory, consists of a box with an aperture that behaves like an ideal emitter: temperature uncertainty 0.3 °C and nominal emissivity 0.98. The calibration of the infrared camera has been performed imposing different temperature to the black body and acquiring the thermal image of the opening by means of the camera NEC TH 7102.

To determine the corrective factor, the temperature of the black body has been set considering the range between 40°C and 100 ° C with a step of 5 ° C and for each value, a thermal image of the black body has been taken. The test has been repeated with 4 cycles. The distance between the infrared camera and the black body of 30 mm has been taken (Figure 17).

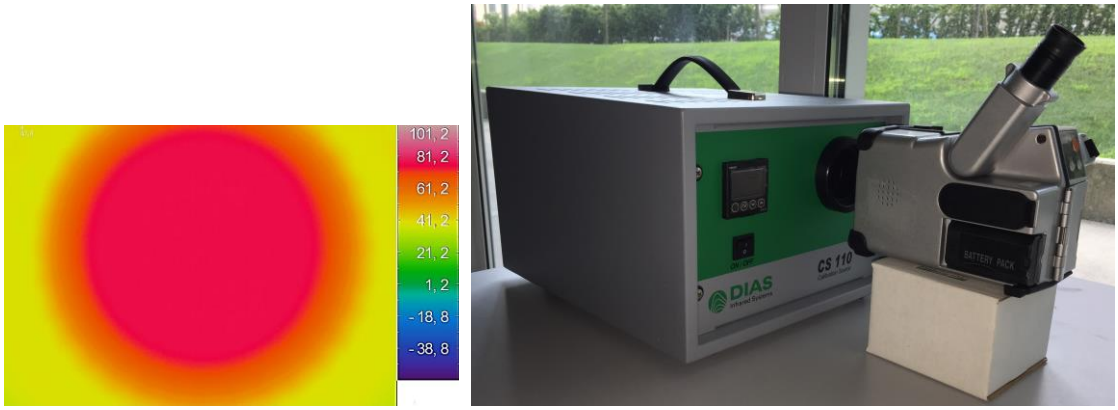

Figure 17 On the right the setup to calibrate the infrared camera, on the left the thermal image of the black body hole.

The experimental procedure, aimed to determine the corrective factor, consists in the following phases:

- Set the temperature to the black body and wait until the steady state condition is reached (the emissivity of the black body is fixed to 0.98).
- Take the thermal image of the hole by using the infrared camera imposing the emissivity equal to 1.
- Analyze the thermal image evaluating the average, the minimum and maximum temperatures within the area of the BB by means of the software InfrRec analyzer.
- Finally compute the corrective factor Fc.

The computation of the Fc value is obtained imposing a power equilibrium between the thermal power measured by the infrared camera (W_{th}) and the black body (W_{bb}). In the following, the equation is explained:

$$W_{th} = W_{bb} \tag{3.1}$$

$$F_C\ \sigma\ \varepsilon_{th}\ T_{th}^4 = \ \sigma\ \varepsilon_{bb}\ T_{bb}^4 \tag{3.2}$$

Simplifying the Stephan-Boltzmann constant, the corrective factor has been computed as:

$$F_C\ 1\ T_{th}^4 = \ 0.98\ T_{bb}^4 \tag{3.3}$$

$$F_C = \frac{0.98\ T_{bb}^4}{1\ T_{th}^4} \tag{3.4}$$

Finally, the coefficients Fc that best fits the data in a least-squares sense has been found using the Polyfit and Polyval functions in Matlab (ANNEX A). The third order polynomial model is described in the equation 3.5 and plotted in the Figure 18.

$$Fc(T) = 4.71E^{-7}x^3 - 1.08E^{-4}x^2 + 8.31E^{-3}x + 0.802 \tag{3.5}$$

To determine the uncertainty, the residual sum of square has been computed [27], following the equation 3.6:

$$u_{Fc} = \sqrt{\frac{\sum_{i=1}^{n}[y_i - y(x_i)]^2}{n - \rho}} \tag{3.6}$$

where y_i is the acquired data, $y(x_i)$ is the value obtained from the polynomial model, n is the total number of data and ρ is the polynomial order +1. Thus, the uncertainty of the corrective factor has been determined to be 0.0028825.

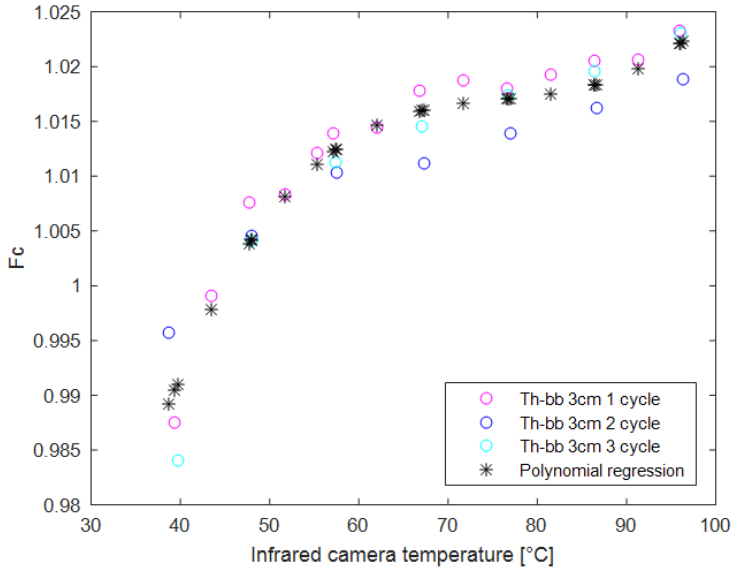

Figure 18 Computed corrective factor and the polynomial regression

3.1.2 Emissivity materials characterization

3.1.2.1 Setup description and characterization of the material emissivity

Because of the small crystal thickness, two orders of magnitude smaller than the diameter, and low thermal conductivity of the quartz any contact resistance thermometer would generate large insertion errors. Moreover any defect, scratch or dirt on the crystal can significantly alter the principal vibration mode i.e. the QCM output. Therefore, a non-contact measurement must be performed to experimentally determine the temperature distribution on the crystal. For this purpose, an infrared camera, NEC TH 7102, has been used. Thermal imagers ideally measure the emitted intensity [W/m^2] of a surface that depends on the temperature according to the Stefan-Boltzmann law:

$$W = \varepsilon\sigma T^4 \tag{3.7}$$

where ε is the emissivity, σ is the Stefan-Boltzmann constant [5.67 10^{-8} W/(m^2 K^4)] and T is the absolute temperature. In order to derive the temperature from the above relationship, the emissivity for each different materials on the crystal must be determined. Being of outmost interest the temperature distribution on the electrode surface, the gold film plating has been removed to allow for the recording of temperature mappings. For this operation,

a chemical solvent ("acqua regia") has been used. It is a mixture of one part of nitric acid and three of hydrochloric acid whose formula is shown below:

$$HNO_{3+3}HCl \tag{3.8}$$

The crystal has been prepared by covering the heater and the resistors, where the film of gold was required, with some grease. In this way, the deposited reagent drop was located in the electrode area only. Leaving the solvent for few minutes, it has been possible to remove the gold, as shown in the Figure 19:

Figure 19 the crystal before (left) and after (right) the gold removal

Thus the emissivity for:

- the electrode material once the gold has been removed,
- the quartz and
- the gold itself

have been determined. The experimental procedure, aimed at measuring the crystal's emissivity, consist of the following phases:

1. Uniformly heating a QCM crystal sample;
2. Measuring the reached (real) temperature with a low uncertainty thermometer;
3. Using IRT to detect radiation emitted;
4. Developing a model to compare the IRT data and the real temperature, in such a way that the emissivity is the only unknown.

3.1.2.2 Emissivity computation

The Figure 20 illustrates the equipment used. The crystal has been placed on the heating mat fed with 10 V by using the power supply. The sample has been fixed on a conductive plate by means of some thermal grease, so that temperature uniformity is achieved between plate and crystal. Moreover, the plate has been surrounded with a baffle in order to block external disturbances though radiation reflection.

The basic idea is that if steady state condition is reached, the conductive plate and the crystal above it, are in thermal equilibrium i.e. they are at the same temperature. The latter has been measured. A 4-wire resistance (PT 100 A-class) has been used to measure the

temperature, converting the output resistance into a temperature value by means of the Calibration table for PT100 resistance thermometers according to IEC 60751 standard.

The NEC TH7102 camera (Resolution 0.06°C (at 30°C), Precision ±2°C/ ±2% of FS and temperature range from -40°C to 500°C) has been used to detect radiation emitted by the heated sample. Figure 20 shows the image of the heated crystal sample from the infrared camera:

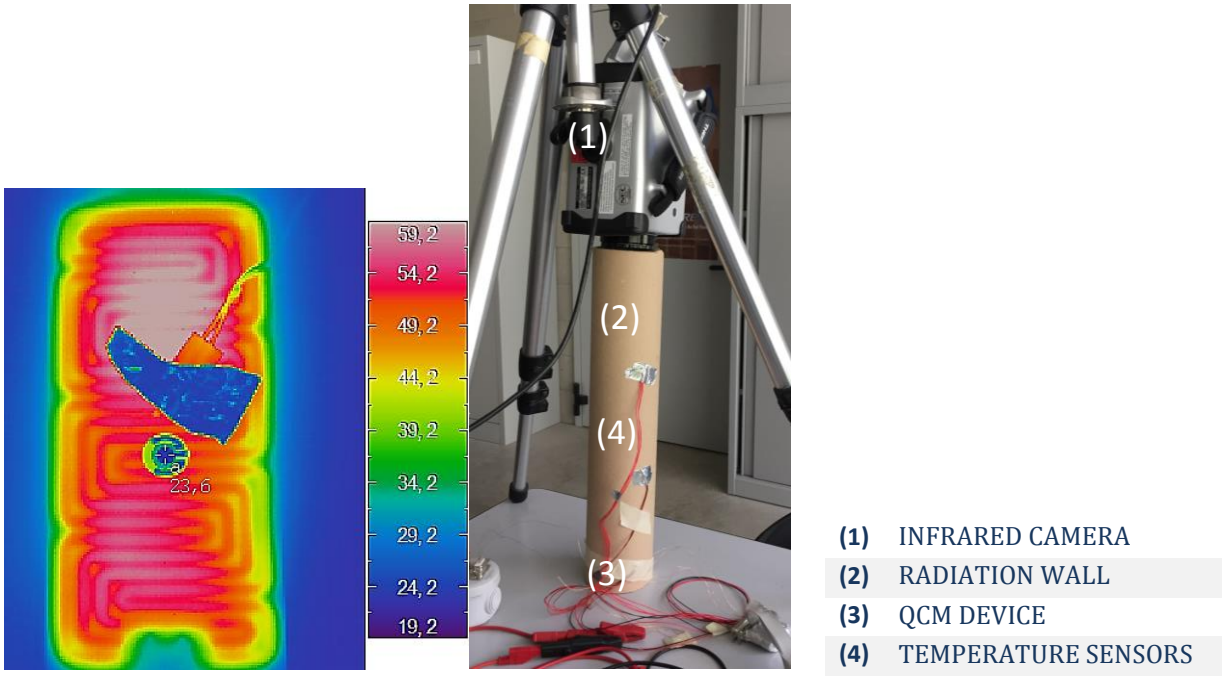

Figure 20 The setup and the thermal image for the emissivity computation.

During the test and the analysis of the thermal image, three assumptions have been made:

1. The atmosphere corrections is not introduced, because the sensing device and the sample have been insulated by an external cardboard cylinder and put close enough (35 cm) so that air transmissibility could be considered unitary [28].
2. Uniform temperature of the crystal is assumed: the emissivity is the only unknown.
3. The crystal is an opaque body
   Considering the power balance when a radiation of power W is impinging on a surface one can write

$$W_{abs} + W_{ref} + W_{tr} = W \tag{3.9}$$

   By dividing both members by W, the following relation is obtained:

$$\alpha + \rho + \tau = 1 \tag{3.10}$$

   where α, ρ and τ are respectively the absorption, reflection and transmission coefficients. The sample is assumed to behave as a perfect opaque surface [29] so that τ is set to zero. Therefore,

$$\alpha + \rho = 1 \tag{3.11}$$

Introducing the Kirchhoff's law:

$$\varepsilon(T) = \alpha(T) \tag{3.12}$$

The equation states that the emissivity and absorption coefficients can be considered equal given that there is no high temperature difference between the surface absorbing energy and the radiation source. In the experiment since the temperature difference is below 100 °C, Kirchhoff law can be applied with no need to correct it. With these assumptions, the reflection coefficient is expressed as a function of the emissivity, giving the following result:

$$\rho = 1 - \varepsilon \tag{3.13}$$

Therefore, with the previous assumptions, the following power equilibrium has been written:

$$\sigma\varepsilon_{th}T_{th}^4 = \sigma\varepsilon_c T_c^4 + \sigma(1-\varepsilon_c)T_{bk}^4 \tag{3.14}$$

where the suffix 'th' refers to the infrared camera, 'c' to the crystal and 'bk' to the background. The first member quantifies the radiation sensed by the infrared camera. The second member is the sum of two contributions: the power directly emitted by the crystal and the one coming from the background then reflected. Simplifying the Stefan-Boltzmann constant and assuming ε_{th} unitary, the only unknown is the sample emissivity. Therefore,

$$\varepsilon_c = \frac{T_{th}^4 - T_{bk}^4}{T_c^4 - T_{bk}^4} \tag{3.15}$$

This equation has been used to extract the emissivity values from the acquired thermal image and using the corrective factor that has been computed during the calibration.

$$\varepsilon_c = \frac{F_c T_{th}^4 - T_{bk}^4}{T_c^4 - T_{bk}^4} \tag{3.16}$$

To evaluate the emissivity uncertainty, the uncertainties of the involved parameters have been identified and summarized below:

- The corrective factor uncertainty considering the previously computed uncertainty of 0.0028825.
- The background and the crystal temperatures uncertainties that depend on the uniformity distribution temperatures along the cylinder (the external baffle) and around the crystal. Both are measured using the 4-wire resistance temperature sensors: three for the background and two for the crystal. The uncertainties have been determined computing the standard deviation (equation 3.17) and finally applying the standard deviation of the average (equation 3.18):

$$S^2 = \frac{\sum_{i=1}^{n}(x_i - \bar{x})^2}{n-1} \tag{3.17}$$

$$S_{\bar{x}} = \overline{S^2} \tag{3.18}$$

Table 2 The involved parameters uncertainties in order to compute the total emissivity uncertainty.

	UNCERTAINTY
CRYSTAL	0.3169 °C
BACKGROUND	1.1486 °C
CORRECTIVE FACTOR	0.002883

In order to propagate the uncertainty from temperatures to emissivity, the hypothesis of independence of the three measured temperature is assumed. Then, the following formula has been applied [27]:

$$u_\varepsilon = \sqrt{\left(\frac{\partial \varepsilon}{\partial T_{bk}} u_{Tbk}\right)^2 + \left(\frac{\partial \varepsilon}{\partial T_c} u_{Tc}\right)^2 + \left(\frac{\partial \varepsilon}{\partial F_C} u_{Fc}\right)^2} \tag{3.19}$$

where u_ε is the emissivity overall uncertainty u_{Tbk}, u_{Tc}, u_{Fc} are respectively the uncertainties of background, crystal temperatures and the corrective factor. The partial derivatives in equation 3.19 can be analytically computed:

$$\frac{\partial \varepsilon}{\partial T_{bk}} = \frac{4\,T_{bk}^3 (F_C T_{th}^4 - T_C^4)}{(T_C^4 - T_{bk}^4)^2} \tag{3.20}$$

$$\frac{\partial \varepsilon}{\partial T_C} = -\frac{4\,T_C^3 (F_C T_{th}^4 - T_{bk}^4)}{(T_C^4 - T_{bk}^4)^2} \tag{3.21}$$

$$\frac{\partial \varepsilon}{\partial F_C} = \frac{T_{th}^4}{T_C^4 - T_{bk}^4} \tag{3.22}$$

The emissivity values and the corresponding uncertainties are summarized below:

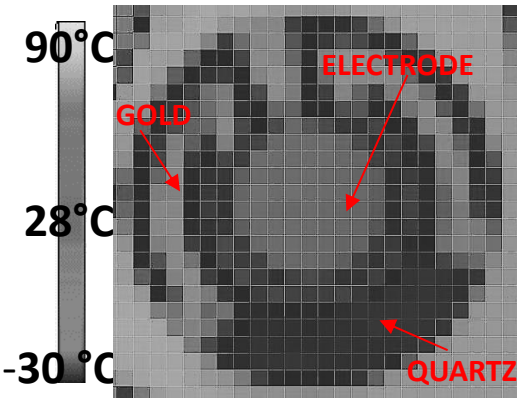

AREA	EMISSIVITY	UNCERTAINTY
ELECTRODE	0.254	0.0067
QUARTZ	0.629	0.0055

AREA	EMISSIVITY
GOLD	0.03

Figure 21 Emissivity average values and the uncertainties for the different materials.

3.2 Thermal gradient identification

After having characterized the emissivity, the infrared camera has been used to determine the thermal fields on the crystal while it was heated by the built-in heater.

3.2.1 Setup description

To determine the thermal gradient, firstly the crystal has been mounted on the structure that allows connecting the deposited resistances with the devices. The structure is equipped with connection wires that are explained in the scheme below:

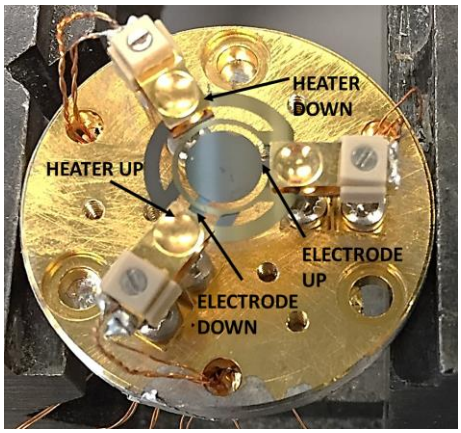

CONNECTIONS	DEVICES
RTD UP	MULTIPLEXER
HEATER DOWN	POWER SUPPLY
ELECTRODES	FREQUENCY COUNTER

Figure 22 Setup devices and connections

There are two deposited geometries: one is used as heater, the other as RTD. These are fixed on the microbalance, one for each flat surface. In order to acquire the required data the wires from the two electrodes have been connected to an electric circuit. This system feeds the crystal with a voltage of ±5 V exciting it at the natural frequency and allowing its measurement. Then, the upper heater (in the Figure 22) has been connected to the

multiplexer that measures the resistance. Finally, the bottom heater has been used as heater fed with a power supply when the thermal gradient needs to be generated.

Once completed the setup, the camera has been placed perpendicularly to the surface of the crystal at the distance of 35 cm. The cylinder has been used to guarantee the insulation from the external radiation. The background temperature has been measured by using three different Platinum resistance thermometer PT100 placed along the height of the cylinder and acquired by the multiplexer.

3.2.2 Measurement of the temperature gradient and its direction

The test has been performed providing a voltage of 20 V (0.022 A) to the heater by means of the power supply. Once the steady state has been achieved, the thermal image has been taken and analyzed using the Matlab code (ANNEX B), imposing the computed material emissivity (quartz, electrodes and gold) and the IR corrective factor. The results of the test are shown below:

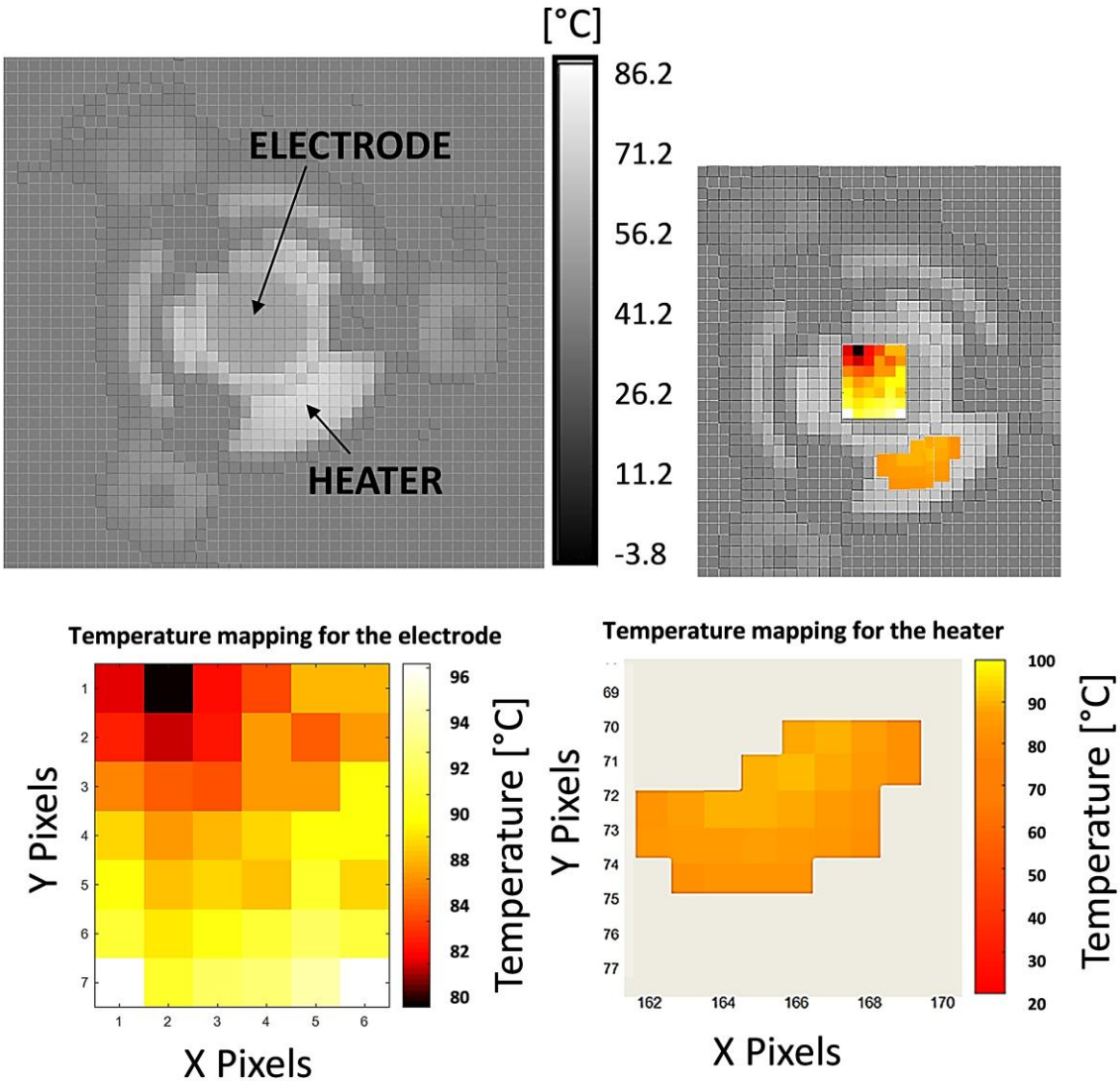

Figure 23 Temperature mapping for the electrode and the heater analysed using the Matlab code.

The map of temperature data follows the same steps discussed in section 3.1.3. The thermal model has been used in the Matlab code. The applied equation is reported hereafter:

$$T_C = \sqrt[4]{\frac{T_{th}^4 - (1-\varepsilon_c)T_{bk}^4}{\varepsilon_c}} \tag{3.23}$$

where:

- T_C is the computed temperature for each pixel from the Matlab code,
- $T_{th}$is the thermal image analyzed by using the thermal image analyzer that allows saving the image as a matrix of temperature,
- $T_{bk}$is the temperature of the background computed as an average value from the three PT100 data, collected by the multiplexer and
- ε_c is the computed emissivity.

Figure 23 shows the resulting temperature field. The maximum temperature reached is approximately 96 °C, while the minimum one is around 80 °C for the electrode. There is a thermal gradient toward the crystal center, which is visible as brighter area in the middle of the image.

To compute the temperature uncertainty (referring to the specific case in the Figure 23), the propagation according to ISO-GUM has been applied. The derivatives of equation 3.23 with respect to the variables T_{th}, ε_c and T_{bk} have been evaluated below:

$$\frac{\partial T_C}{\partial T_{th}} = \frac{T_{th}^3}{\varepsilon_c \sqrt[4]{\left(\frac{T_{th}^4 - (1-\varepsilon_c)\,T_{bk}^4}{\varepsilon_c}\right)^3}} \tag{3.24}$$

$$\frac{\partial T_C}{\partial \varepsilon_c} = \frac{T_{bk}^4 - T_{th}^4}{4\,\varepsilon_c^2 \sqrt[4]{\left(\frac{T_{th}^4 - (1-\varepsilon_c)\,T_{bk}^4}{\varepsilon_c}\right)^3}} \tag{3.25}$$

$$\frac{\partial T_C}{\partial T_{bk}} = \frac{(1-\varepsilon_c)\,T_{bk}^3}{\varepsilon_c \sqrt[4]{\left(\frac{T_{th}^4 - (1-\varepsilon_c)\,T_{bk}^4}{\varepsilon_c}\right)^3}} \tag{3.26}$$

To propagate the uncertainty [27] the following relationship has been applied:

$$u_{Tc} = \sqrt{\left(\frac{\partial T_C}{\partial T_{th}} u_{Fc}\right)^2 + \left(\frac{\partial T_C}{\partial T_{bk}} u_{Tbk}\right)^2 + \left(\frac{\partial T_C}{\partial \varepsilon_c} u_{\varepsilon_c}\right)^2} \tag{3.27}$$

The results are summarized in the Table 3:

Table 3 Uncertainty results.

$\overline{T_{bk}}$	$T_{th\ ele}$	T_{ele}	T_{heater}	u_{Fc}	$u_{T\ bk}$	u_{ε}	$u_{T\ ele}$	$u_{T\ heater}$
[°C]	[°C]	**[°C]**	**[°C]**	-	[°C]	-	**[°C]**	**[°C]**
23.16	43.16	**86.10**	**90.88**	0.0029	0.20	0.0032	**0.85**	**0.42**

3.2.3 Non-uniform temperature effects on the frequency variation

In order to identify the temperature gradient effects on the frequency variation, the experimental activity has been performed, connecting the power supply to the heater on the surface of the crystal and collecting the data. The acquisition has been performed following the steps described below:

- The power supply has been connected to the heater reaching the steady state condition.
- The thermal image has been taken with the infrared camera.
- The upper resistance and the temperature of the background have been collected by using the multiplexer device.
- The frequency has been recorded using the frequency counter synchronized with the multiplexer.

The analysis has been carried-out determining the mean temperature of the electrode and the heater from the thermal image, the frequency variation as a difference between the frequency after the heater on and the value at the ambient temperature. Finally, the temperature of the electrode has been computed knowing the resistance temperature calibration, performed in the section 2.1.

Referring to the thermal image in the Figure 23, the acquired data are summarized in the Table 4:

Table 4 The acquired data for the power supply at 20 V.

T_{bk1}	T_{bk2}	T_{bk3}	$\overline{T_{bk}}$	R	T_R	V	I	Δf	F_{C_el}	T_{ele}	F_{C_he}	T_{heater}
[°C]	**[°C]**	**[°C]**	**[°C]**	**[Ω]**	**[°C]**	**[V]**	**[A]**	**[Hz]**	**-**	**[°C]**	**-**	**[°C]**
23.12	23.16	23.22	23.16	39.76	85.50	20	0.022	1694.50	0.99	86.10	1.016	90.88

The same analysis has been performed with different voltages of the power supply from 10 V to 24 V with a step of 3 V, repeating three cycles. The results are displayed in the following graph (Figure 24).

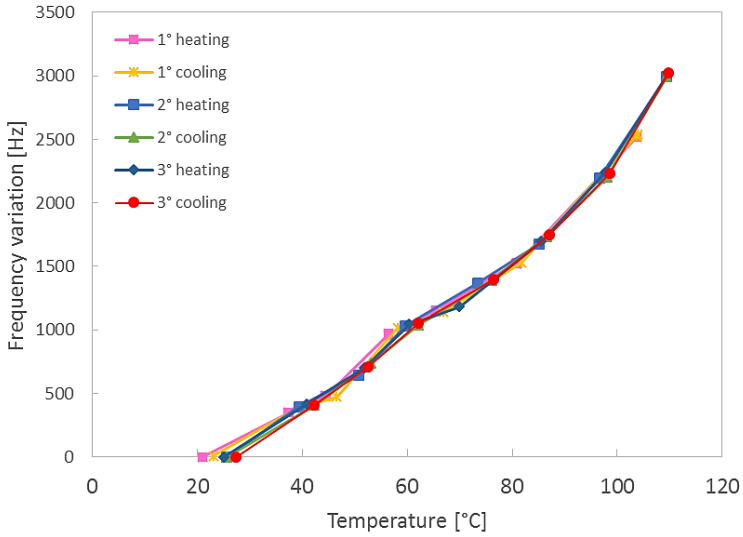

Figure 24 Heater on at different voltage

It can be observed that all the heating and the cooling cycles, at different power levels, are quite overlapping evidencing the repeatability of the effect on the frequency.

Finally, the uniform temperature-frequency variation relationship (the polynomial trend), shown in the Figure 16 in the paragraph 2.3.3, has been plotted on the same graph (Figure 25). A huge gap is evident between the frequency at uniform temperature and that recorded in these tests proving the strong effect of the thermal gradient.

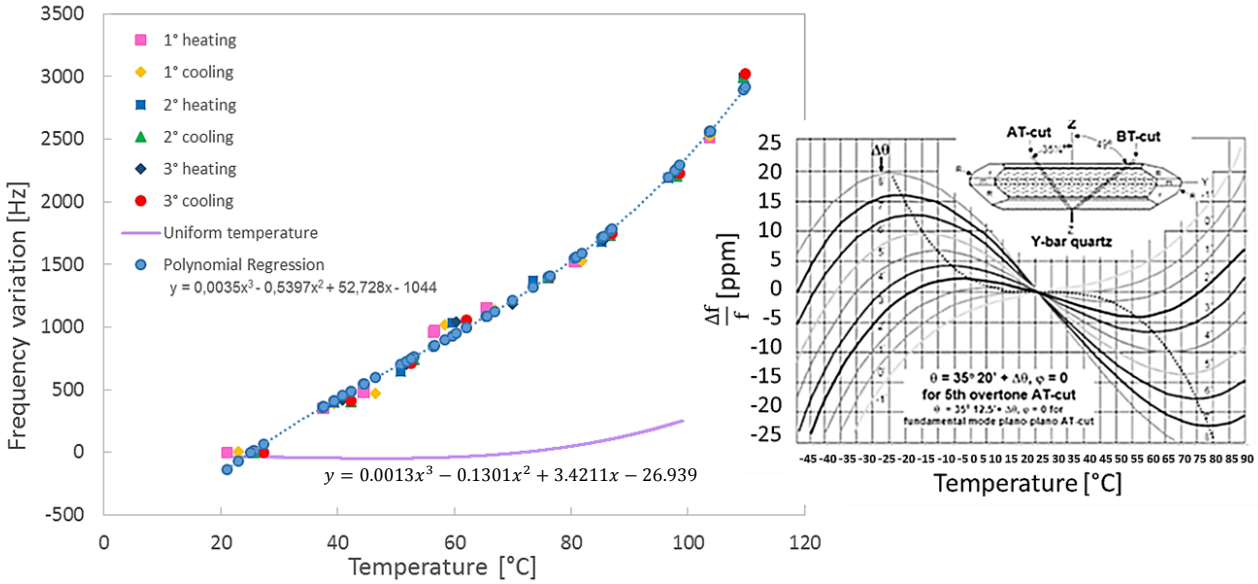

Figure 25 Non uniform vs uniform temperature trend

3.3 Conclusions

The experimental activity has been performed to investigate the temperature filed on the crystal. The infrared camera has been used to measure the temperature gradient recording of temperature mappings. The image results demonstrate that there is a gradient of temperature moving toward the crystal center (in the electrode area).

The thermal gradient effect on the frequency variation have been identified with the experimental activity and the results have been compared with the uniform temperature-frequency variation relationship. A huge gap is present between the frequency change at uniform temperature and the one recorded in these tests at the same average temperature but under a strongly non uniform thermal field; this evidences the strong effect of the thermal gradients.

3.4 Thermal analysis to compute the temperature gradient

In the following section, the thermal model of the crystal is presented. The FEM model has been developed to compute the temperature field and correlate it with the tests described in the previous paragraphs 3.1-3.2.

3.4.1 Thermal Model

The thermal model is shown in the Figure 26.

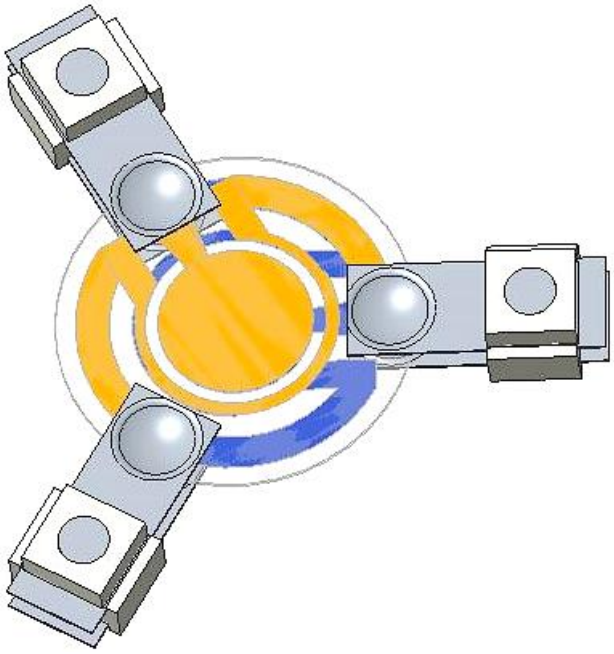

Figure 26 The 3D model

The model has been designed considering the crystal placed between the blades of the support. For the thermal analysis, another important point to consider has been the contact of crystal and supports. In the model, it has been simulated as bonded surfaces between the flattened surface of the blades, upper and lower, and the crystal-contacted area. This solution allows, in thermal mode, to automatically create a conductive link over the bonded interfaces.

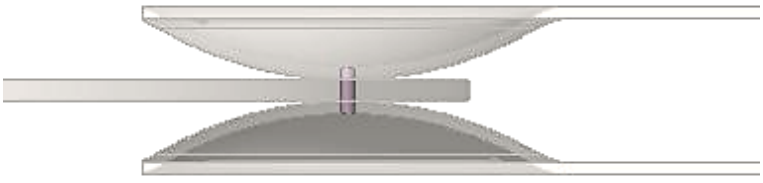

Figure 27 Bonded surfaces between the crystal and blades

In order to perform the analysis three different material have been simulated; the quartz has been assigned to the crystal, the stainless steel AISI316 to the supports and finally the plastic material, Macor, to the spacers. All the materials have been modeled with isotropic behavior. In the Table 5, the material properties are summarized:

Table 5 Material properties

COMPONENTS	DENSITY	YOUNG MODULUS	POISSON COEFFICIENT	THERMAL COEFFICIENT	THERMAL CONDUCTIVITY
	[Kg/m^3]	[MPa]		[1/°C]	[W/(m °C)]
QUARTZ	2649	76500	0.17	7.10E-06	6.2
AISI316	8000	193000	0.29	1.60E-05	14
MACOR	2520	66900	0.29	9.00E-06	1.5

3.4.2 Loads

In order to validate the model, the same conditions of the experimental tests (heating power, environmental temperature) have been simulated. The baseline analysis considered a power dissipation on the device of 0.445 W and it was localized in the heater area of the crystal bottom surface. The total heat load has been distributed considering the resistance in each of the different areas of the heater so, not uniformly distributed throughout the heater path. Thus, given a certain current value, the different power heating has been realized dividing the total area in regions, as shown below:

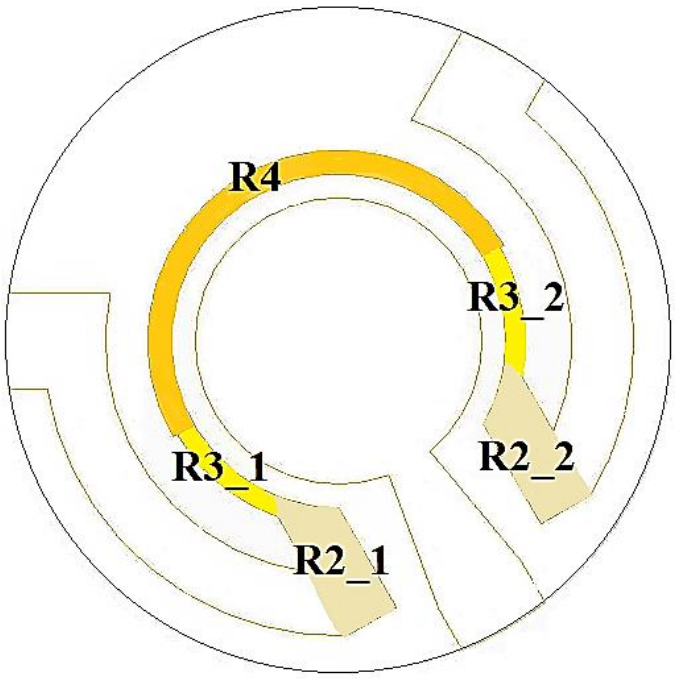

Figure 28 Different heater area in order to identify the resistance

To distribute the heating power on the heater of the crystal, the resistance for each area has been computed. In the model, the heater has been split in smaller areas with a simple geometry as shown in the Figure 28. For each part of the heater, the lengths and areas have been measured: for the length has been considered the average arch while for the area the transversal one, rectangular by construction.

The resistances have been computed according to the following formula:

$$R = \rho \frac{l}{A} \tag{3.28}$$

where l and A are respectively the length and the transversal area and ρ is the resistivity. Once defined the resistances, in order to compute the power heating for each area the following formula has been given:

$$\dot{Q} = \dot{Q}_1 + \dot{Q}_2 + \dot{Q}_3 \tag{3.29}$$

$$\frac{R_{TOT} I^2}{R_{TOT}} = \frac{R_1 I^2 + R_2 I^2 + R_3 I^2}{R_{TOT}} \tag{3.30}$$

Knowing the current I and the Resistance R (previously computed) the power heating for each area has been obtained as:

$$\dot{Q}_1 = \frac{R_1 I^2}{R_{TOT}} \tag{3.31}$$

The results of the computation are summarized in the Table 6:

Table 6 Parameters and heat loads computations

RESISTIVITY [Ohm]	0.00000083				
THICKNESS [m]	0.00000016				
	R2_1	**R3_1**	**R4**	**R2_2**	**R3_2**
LENGTH [m]	0.00298	0.00239	0.0118	0.00298	0.00239
AREA [m²]	2.288E-10	6.4E-11	8E-11	2.288E-10	6.4E-11
RESISTANCE [Ohm]	10.818	31.109	122.522	10.818	31.109
TOTAL R [Ohm]	206.376				
R/R tot	0.0524	0.151	0.594	0.0524	0.151
CURRENT [A]	0.0254				
POWER $\dot{Q}$ [W]	**0.0233**	**0.067**	**0.264**	**0.0233**	**0.067**
TOTAL POWER [W]	0.445				

3.4.3 Boundary conditions

In order to perform the thermal analysis, the required constrains have been identified as the convection and the radiation coefficients and the temperature of the spacers. The convection coefficient has been computed considering the equation 3.32 and assuming the crystal equal to a horizontal plate in air:

$$h_{conv} = C_1 \left(\frac{f \, \Delta T}{M} \right)^{1/4} \tag{3.32}$$

where ΔT is the difference of surface and environment temperatures [K], f is the so-called relative pressure factor (equal to one since the test was performed in air), M is the area to perimeter ratio; C1 is a constant and is given in tabular form. Because of the flow has been assumed turbulent, the constant is equal to 1.71 [30].

Table 7 Parameters to compute the convection coefficient

PARAMETERS	[°C]	[K]
T heater	90.88	364.03
T electrode	86.10	359.25
T from R	85.50	358.65
T air	23.16	296.31
C1		1.71
f		1
AREA [m²]		0.00015
PERIMETER [m]		0.044
M		0.0035

In the model, convection constraints have been inserted both to the top and the bottom surface of the crystal. From the previous parameters, the convection coefficient has been computed equal to 19.8 W/(m² K).

Considering the radiation coefficient makes the model non-linear. However, both radiation and convection constraints have to be applied to the same surfaces and the software allows only one condition for each surface to be set. For this reasons, the radiation constraint has been linearized. The procedure is based on the reduction of the radiation coefficient to a difference of two squared quantities. Starting from the equation:

$$W = \sigma \varepsilon A (T_w^4 - T_\infty^4) \tag{3.33}$$

It becomes:

$$W = h_r A (T_w - T_\infty) \tag{3.34}$$

and *hr* is the linearized radiation coefficient, given by the following expression

$$h_r = \sigma \varepsilon (T_w^2 + T_\infty^2)(T_w + T_\infty) \tag{3.35}$$

The *hr* coefficient assumes a different value corresponding to the different emitting materials. In the model, the radiation from the supports has been neglected since the latter are plated with gold and have a very low emissivity.

In order to compute the radiation coefficient, the temperatures and the emissivity values are summarized in the Table 8:

Table 8 Parameters used during the computation

PARAMETERS	[°C]	[K]
T heater	90.88	364.03
T electrode	86.09	359.25
T from R	85.49	358.65
T air	23.16	296.31
σ [W/(m² K⁴)]		5.67E-08
ε QUARTZ		0.63
ε ELECTODE		0.25
ε GOLD		0.03

The computed radiation coefficients are showed in the Table 9:

Table 9 Computed radiation coefficient

Radiation Coefficient	[W/(m²K)]
h_r quartz crystal top	5.06
h_r quartz crystal bottom	5.06
h_r electrode top	2.05
h_r electrode bottom	0.24

Finally, the global heat exchange coefficient has been computed by summing the convection and the radiation coefficients, as in the equation 3.36:

$$h = h_{conv} + h_r \tag{3.36}$$

The summary of the complete constraints simulated in the model are described in the Table 10:

Table 10 Constraint coefficient for the FE model

CONSTRAINTS	[W/(m²K)]
h quartz crystal top	24.8
h quartz crystal bottom	24.8
h electrode top	21.8
h electrode bottom	20.0

The last constrains imposed to the model has been the prescribed temperature of the supports' spacer. The values have been computed considering the proper emissivity (plastic material, Macor, equal to 0.85) and the corrective factor from the calibration of the infrared camera. In the picture, the different values for the three supports are displayed in the Figure 29:

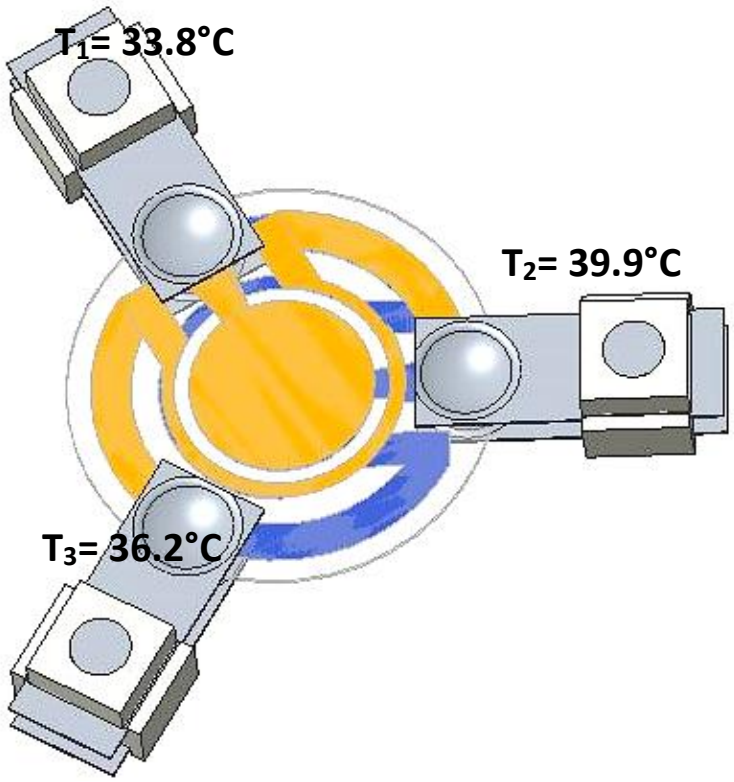

Figure 29 The prescribed temperature of the supports' spacer

3.4.4 Results

3.4.4.1 Thermal analysis results

In the following (Figure 30), the thermal analysis results are displayed:

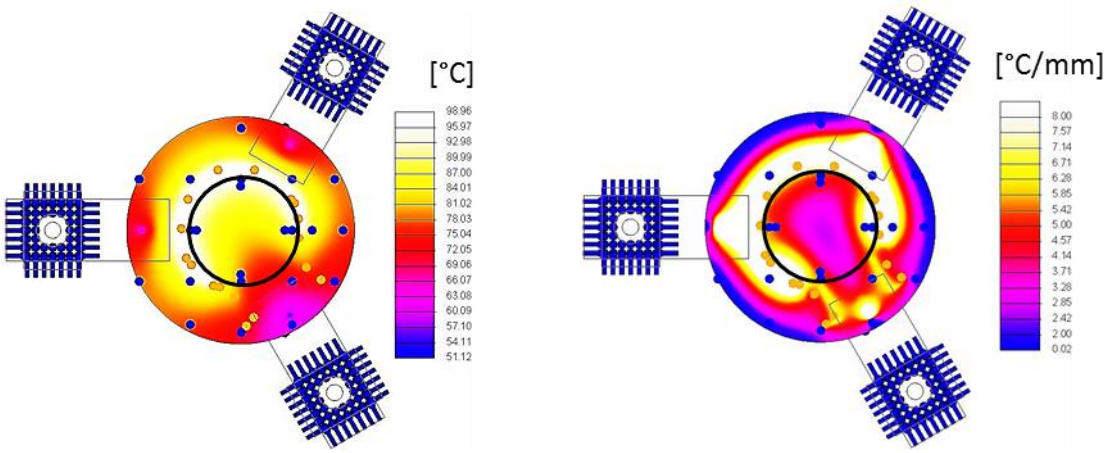

Figure 30 The electrode temperature mapping on the left and the temperature gradient on the right.

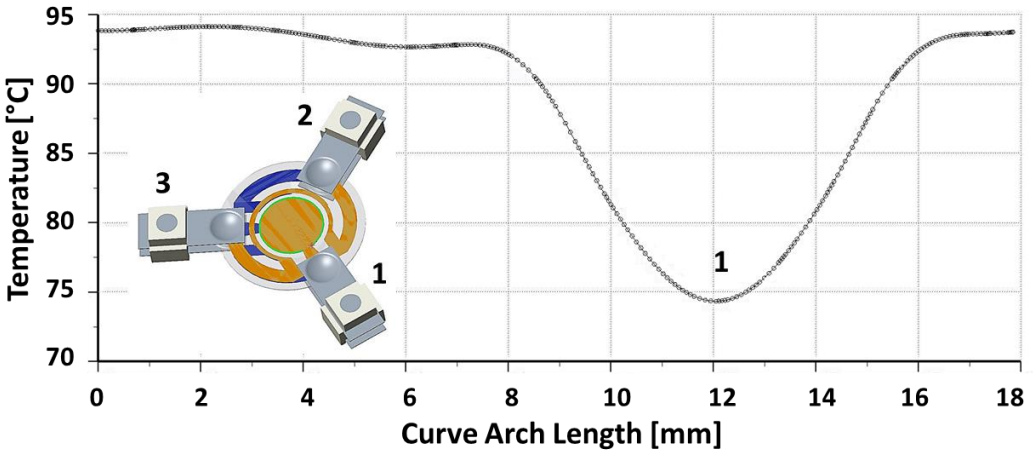

Figure 31 Temperature profile on the electrode edge.

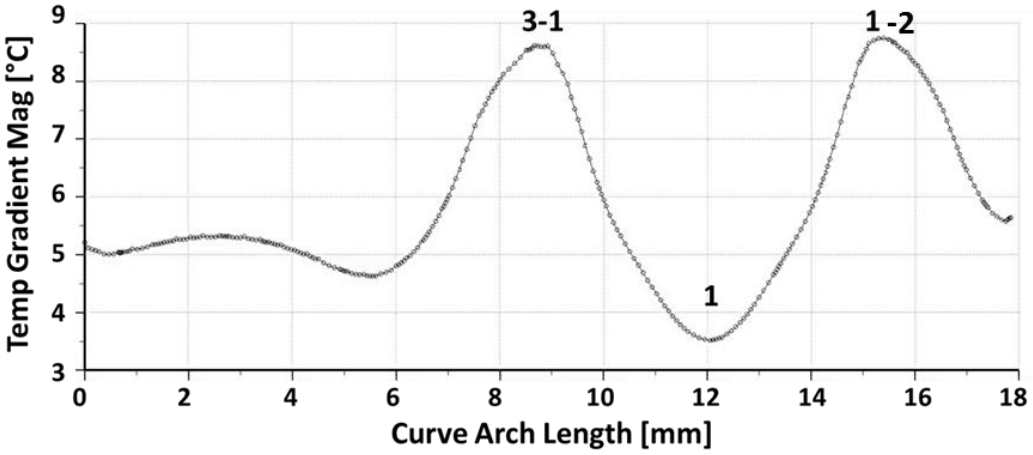

Figure 32 Temperature gradient magnitude on the electrode edge.

The graph, in Figure 31, shows the temperature profile of the electrode edge. It can be noticed that the lower temperature value is reached in correspondence of the support 1 (shown in the figure). The latter is consistent with the observation that this area is the farthest from the active heater on the crystal. Considering the second graph, Figure 32, the maximum flow is between the contact points 1-3 and 1-2, where the heat generated by the heater is distributed on the points of the surface. Whereas, the minimum on the electrode is where there is no heat dissipation from the heater and where the support 1 removes the heat.

Furthermore, the thermal field is symmetric with respect to an axis passing through the centre of the disk surface and rotated of 60° from the x-axis (Figure 33). It can be noted that the areas of highest temperature are the ones of the heater. This is expected since those areas receive a direct heat load. The supports have the lowest temperature, 34 °C. Concerning the crystal, the lowest temperature is around 68 °C. This value is reached on the regions of contact with the three supports where heat is dissipated through conduction.

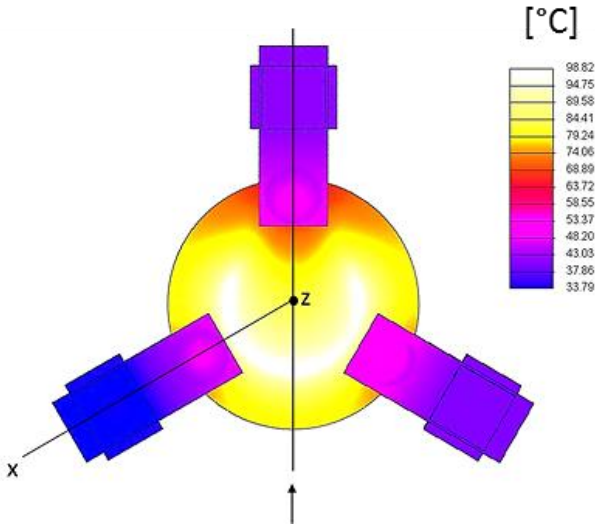

Figure 33 The thermal field symmetry.

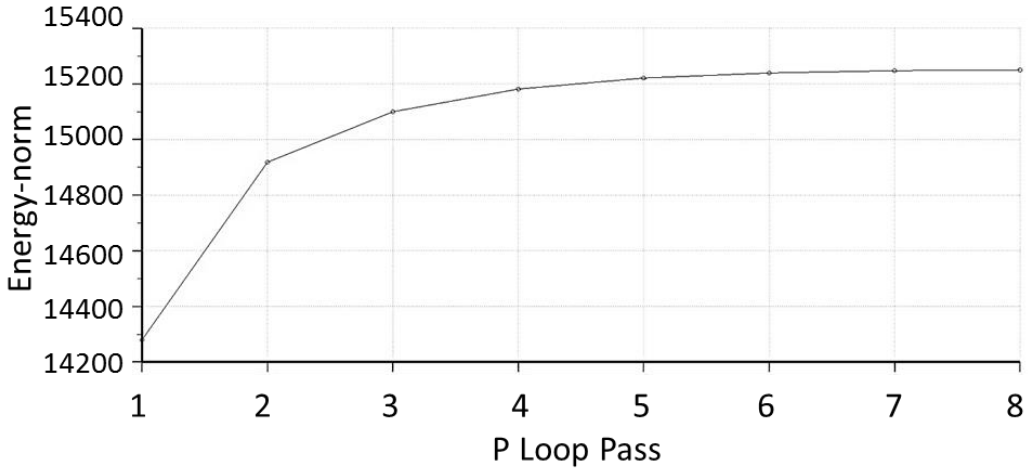

Figure 34 Convergence graph of the model

Finally, the convergence of the analysis has been checked. The global energy norm reaches a steady value after increasing the functions' order up to five (Figure 34). This means that the result approaches the unique model solution.

3.4.4.2 Comparison results

The thermal field from the thermal analysis (CREO model) has been compared with the measured one (with MATLAB computation). Five points of the electrode have been identified on the model and compared with the temperature map obtained experimentally. The same has been done for the heater considering four points to be compared.

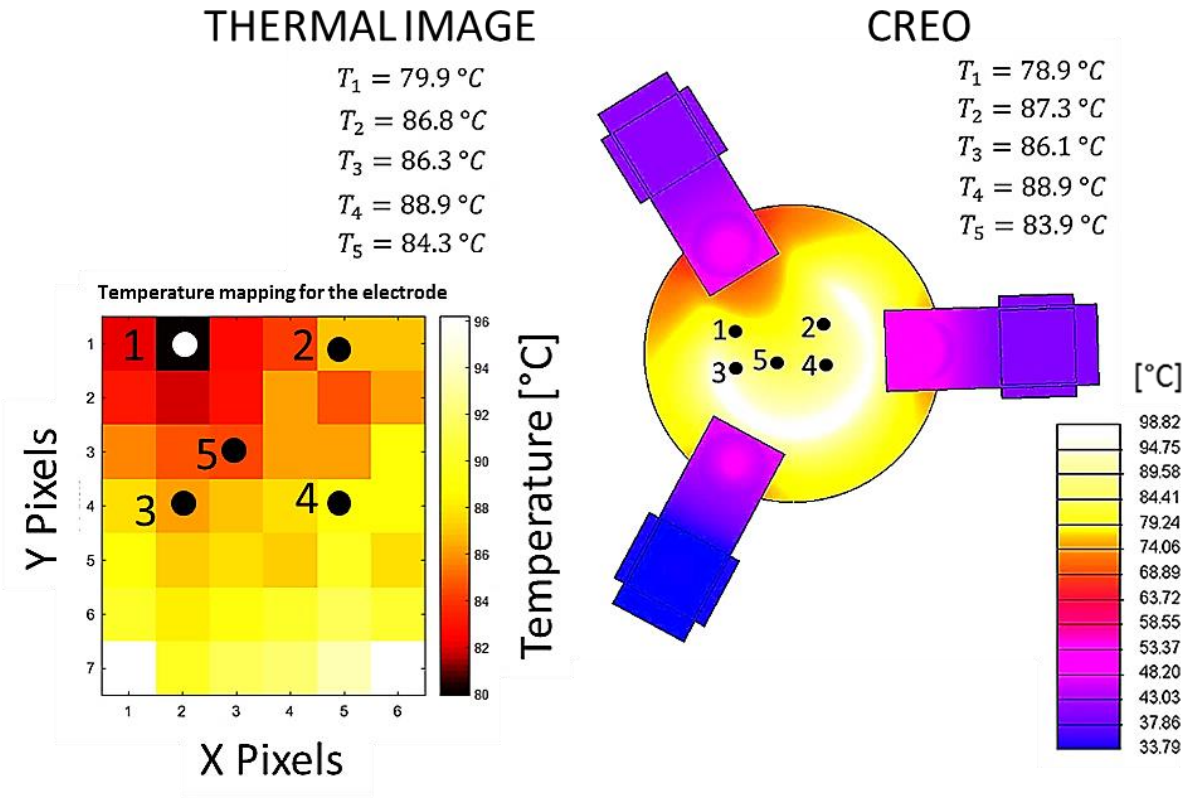

Figure 35 The temperature results for the electrode, computed with the thermal analysis (CREO model on the right) and experimentally (MATLAB on the left)

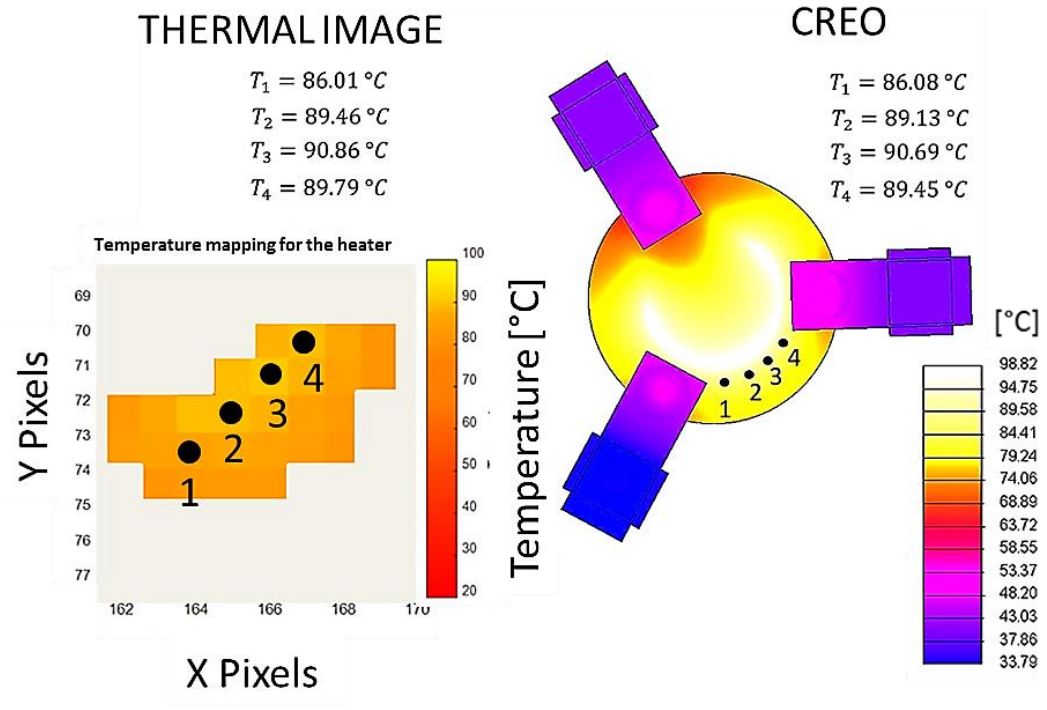

Figure 36 The temperature results for the heater, computed with the thermal analysis (CREO model on the right) and experimentally (MATLAB on the left)

Table 11 Comparison results error on the electrode and heater temperature values.

Electrode points	Error [°C]
1	1
2	-0.5
3	0.2
4	0
5	0.4

Heater points	Error [°C]
1	-0.07
2	0.33
3	0.17
4	0.34

The temperature measured with the experimental test (analysed with MATLAB) and those predicted by the thermal model are quite close: the maximum error on the electrode temperature is 1 °C, while the one on the heater is 0.34 °C.

3.5 Conclusions

From the thermal analysis, the temperature profile of the electrode edge shows that the lower temperature value is reached in correspondence of the farthest area from the active heater on the crystal. Accordingly, the maximum flow is where the heat generated by the heater is distributed on the points of the surface: the minimum on the electrode is where there is no heat dissipation from the heater and where the colder support removes the heat. Comparing the thermal model with the numerical results, the temperature values are quite close with errors lower than 1°C. Thus, it can be concluded that the thermal model has been validated and it allows for a more detailed analysis of the thermal filed because it is not limited as the thermal image by a fixed spatial resolution.

CHAPTER 4

4 FEM MODEL FOR TSM ANALYSIS

The effects of temperature on the microbalance has been analysed also by using the FEM technique to shed light on the effects of a non-uniform thermal field on the thickness shear modes (TSM).

4.1 FEM model

Since the hypothesis of a linear model would not allow evidencing the effect of a thermal-field on the modal behaviour, it has been necessary to define temperature dependent parameters and implement a non-linear model with elastic moduli dependent on the stress. The model was implemented in ABAQUS. Considering the material properties, the anisotropic behaviour of quartz has been introduced. The elastic matrix at reference temperature and no stress has been implemented as follows:

$$E = \begin{bmatrix} 87.49 & 27.07 & -8.93 & 3.36 & 0 & 0 \\ 27.07 & 102.84 & -7.34 & -9.89 & 0 & 0 \\ -8.93 & -7.34 & 130.36 & -5.44 & 0 & 0 \\ 3.36 & -9.89 & -5.44 & 38.73 & 0 & 0 \\ 0 & 0 & 0 & 0 & 29.36 & -2.14 \\ 0 & 0 & 0 & 0 & -2.14 & 69.25 \end{bmatrix} \quad (4.1)$$

There are three different shear moduli associated with this material (the last three values on the main diagonal): the highest one is torsional [5] and the other two (respectively 29.36 and 38.73 GPa) are the ones responsible for TSM. The fact that there are two different thickness shear modes with displacements orthogonal to each other is confirmed by literature [31]. In this study, the lower of the two TSM frequencies has been considered.
In the model displacements orthogonal to the planar crystal's surfaces have been prevented on all crystal's boundaries. This has been done in order to speed-up the analysis by avoiding the extraction of the countless flexural modes that are outside the scope of our analysis.
Finally, the damping has been excluded from the model because the crystal has a high Q factor (see chapter 1 paragraph 1.4). This means that the damping ratio is very small and, for this reason, its effects has been neglected in the analysis. Model non-linearity was expressed by the elastic moduli dependence on the stress.

4.2 Uniform temperature effect

The model behaviour under a constant temperature distribution has been first of all evaluated. A uniform temperature field was expected to produce changes because the density, elastic moduli and geometry, i.e. all the parameters that determine the frequency behavior. The technical literature provides tables with parameters-temperature values. Linear interpolation has been performed between the provided values.

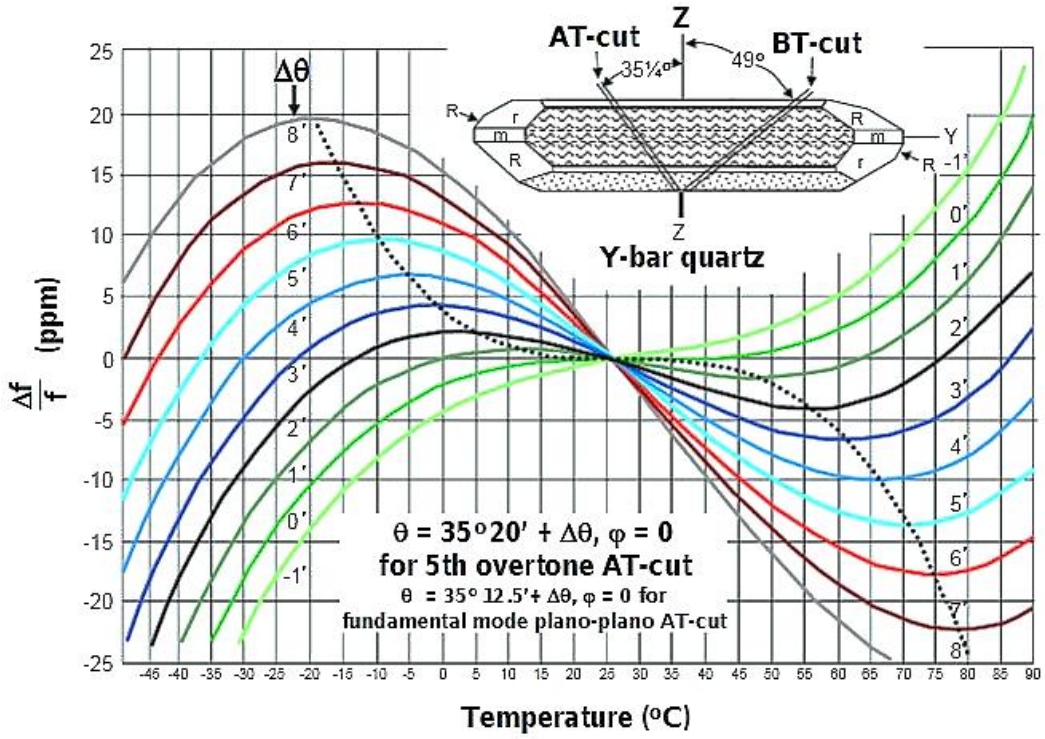

Figure 37 Frequency-temperature curve with different cut angle.

Figure 37 shows an example of frequency-temperature behaviour of an AT-cut quartz crystal. Since the Y-axis values are in ppm, frequency shifts are very small compared to the initial resonant frequency (around 10 MHz in the case under study). For example, a 1 ppm shift corresponds to a variation of the initial frequency of 10 Hz, which ultimately translates into a change in the last two figures of the 10 MHz number. Such a small variation can be difficult to be accurately detected by FEM technique since the latter is prone to numerical errors. For this reason, before starting the analyses, the software has been set to work with double precision numbers in every step of the calculations made. Moreover, a finer mesh with respect to what previously shown, has been used for the occasion. However, even if these preventative measures have been adopted, a high accuracy on the results is not guaranteed a priori.

It should also be noted that the curves in Figure 37 are plotted for different values of the angle of cut. All other variables are kept constant. In this work, a pure AT-cut is under study and this means that ϑ is equal to 35° 15'. Therefore, it is not possible to compare the curve obtained by means of FEM with the one of Figure 37. However, from a qualitative point of view, it can be concluded that the frequency variation should increase with temperature. Moreover, it is known from theory that the curve should be close to a third degree polynomial [13].

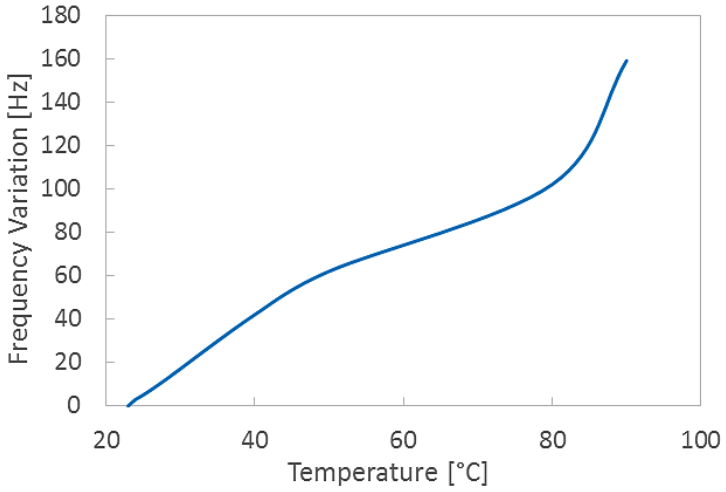

Figure 38 Frequency shift at uniform temperature from FEM analyses.

It can be seen that, while the FEM is able to catch qualitatively the increase in frequency shifts with temperature, the curve is not a third degree polynomial. The reason for this behaviour lays in the approximated nature of the input parameters.
As mentioned earlier, the frequency-temperature curve is (in first approximation) the result of the combined effect of density, elastic coefficients and thickness variations.
It is clear that, in order to get the exact frequency temperature behaviour of Figure 37, the parameters in the equation (and in the FEM model) must be known with a high accuracy. In practice, they are not. First, they are experimentally determined and, therefore, a certain extent of uncertainty in their measurements is present. Second, their relation with temperature is not known in closed form but through a grid of points. Linear interpolation has been used between the intermediate values and this is a strong source of error.
An estimate of the uncertainty on the frequency shift can be computed by using the propagation of uncertainties method already presented in chapter two. The absolute uncertainties of the three parameters can be estimated at respectively $0.005/\sqrt{3}$ GPa, $0.5/\sqrt{3}$ kg/m^3 and $(0.005/\sqrt{3})\cdot10^{-6}$ m. In such a configuration, the uncertainty on the frequency shift has been estimated at around 500 Hz.
Thus, the model has a high sensitivity to the input parameters, and, since the latter are not known with enough accuracy, it is virtually impossible to get exactly a third degree polynomial out of the FEM modal analysis.

Previous tests have shown that the frequency-temperature behaviour of the crystal under study is as shown in the next figure [32].

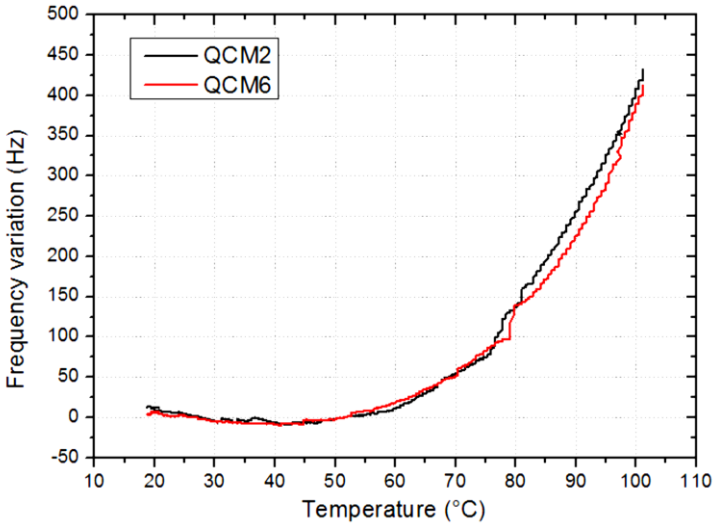

Figure 39 Frequency temperature plot for crystal under investigation

Each point of Figure 39 has been obtained in steady state condition and under a homogeneous temperature field (thermal energy was not delivered from the heater). It can be seen that the crystal shows very small frequency shifts up to 50 °C; this phenomenon is also referred to as temperature compensation. Above this temperature, the curve behaves like a third order polynomial as expected.

The way this kind of crystals are manufactured by either contouring or angle-correction techniques [31]. The basic idea is that a quartz slab is tested in a trial and error process in order to find small corrections of the angle of cut and/or the thickness with the goal of having a frequency-temperature curve like the one in Figure 39. Due to high number of variables involved, the process is repeated for each single quartz slab. The consequence of interest for this thesis is that not even the angle of cut is known with precision. Clearly, this is another source of error.

A comparison of the curve resulting from FEM and the experimental one is shown in the next figure.

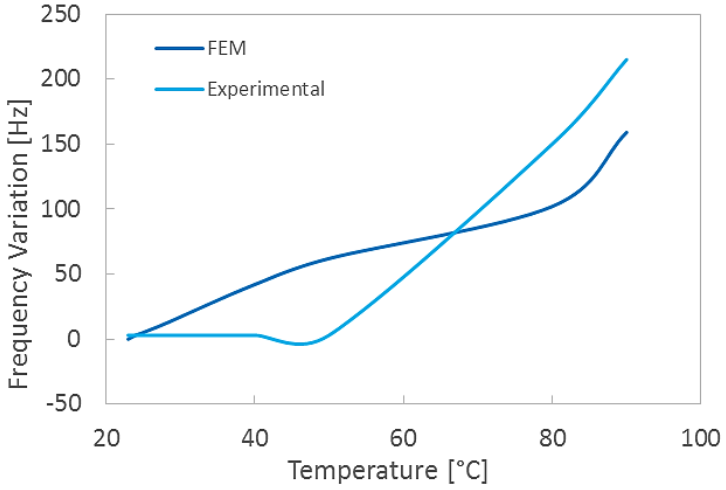

Figure 40 Comparison of FEM curve and experimental one.

It can be seen that the maximum difference is of around 60 Hz of 50 °C. Thus, it is concluded that the FEM errs of maximum 60 Hz.

For the sake of completeness, the FEM capability of reproducing the experimental behaviour has been tested. This served as a further proof of the claim that the FEM inaccuracies are due the input parameters. To do so, density and the elastic matrix have been assumed as precisely known. The thickness has been computed inverting the equation 1.6 with the goal of matching the curve of Figure 39. The obtained curve is shown in the Figure 41.

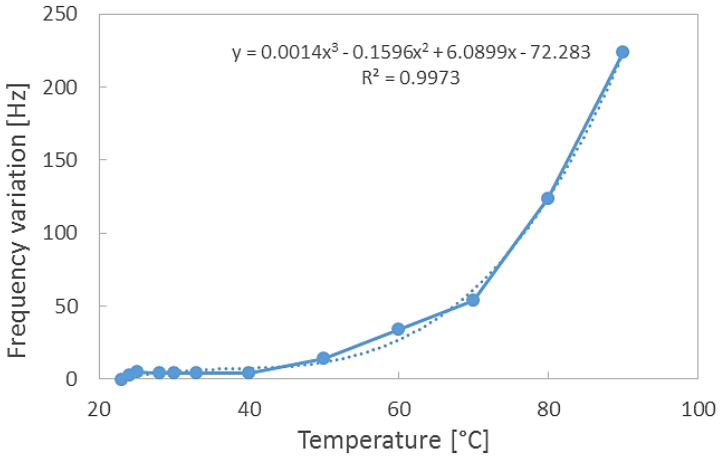

Figure 41 FEM results

It can be seen that the curve is very close to the experimental one. The shape is also very well approximated by a third order polynomial. However, the CTE used in these analyses showed a trend with temperature that is not consistent with what found in literature. This is because the thickness value had to compensate for the errors present in all the other parameters.

This clearly proves that it would be possible in theory to model the frequency-temperature behaviour. However, this is prevented by the errors in the input parameters that are entirely responsible for it.

Thus, the idea of using the temperature field extracted from the thermal analysis has been discarded, because the model did not reproduce the actual microbalance well.

4.3 Thermal gradient effect

The original model has been partitioned to have an inner disk surrounded by an outer ring.

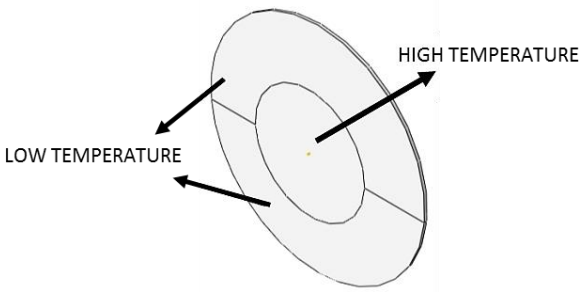

Figure 42 Model for thermal gradient FEM analysis

Material properties at ambient temperature have been assigned to the outer disk, while the rest of it has been supposed to be at 90 °C. The reason for this choice derives from the temperature field of the thermal analysis (Figure 30), where the highest temperature values have been reached in the centre.
The frequency at which the TSM mode happens in this configuration is shown in Table 12:

Table 12 Comparison of the frequency shift with uniform and thermal gradient fields

Thermal fields	Frequency [Hz]
Uniform Temp (23°C)	9935576
Uniform Temp (90°C)	9935735
Thermal grad (23-90°C)	9937420

It can be noted that the frequency at which the disk vibrates in the case of the temperature gradient is much higher than the two uniform temperature cases. In particular, an increase of 1.7 kHz was detected with the 90 °C uniform thermal field. Thus, the frequency shift observed in the last case is one order of magnitude higher than what expected from previous result. This difference has to be an effect of the temperature gradient.

4.4 Conclusions

A finite element model has been developed and tested to foresee the frequency variation-temperature curve under uniform thermal fields. However, some discrepancies has been detected between model and actual device behaviour due to the high uncertainty of elastic coefficients, density, CTE and angle of cut values.
Furthermore, a thermal gradient has been simulated: the computed eigenfrequency was much higher than what detected in the uniform temperature distribution case. Clearly, implemented a correction with the numerical analysis is not a viable solution for the mentioned model inaccuracy therefore, an experimental characterization of the sensitivity to the “temperature gradient” has been carried-out.

CHAPTER 5

5 THERMAL GRADIENT- FREQUENCY VARIATION RELATIONSHIP

In order to determine the QCM sensitivity to the temperature gradients in a normal calibration procedure one should have carried-out the QCM calibration under different values of the gradient. Calibration of the QCM is not an easy task because its mass sensitivity is so high that no reference with appropriate accuracy is available. The thermal gradient measurement is an issue itself because the procedure based on the processing of thermal maps is not applicable to standard QCM that are gold coated behaves like mirrors. What could be done was determining the QCM frequency change generated by different power dissipation of the crystal heater. This produces both different thermal gradients and different average temperatures. Provided that the effect of the average temperature change has been already characterized in the previous chapter, if one assumes that the two effects can be superimposed the effect of the gradient alone can be obtained by removing that of the average temperature. Concerning the assessment of the gradient, once verified the thermal model validity through correlation with the experimental data (Figures 35-36), it has been used as a tool for the gradient assessment. Finally the thermal gradients has been related with the effect of frequency variation obtained experimentally. One should anyway remark that if the thermal gradient besides having an additive effect changed also the mass sensitivity our procedure could not evidence it.

5.1 Thermal power loads simulated on the model

Considering the thermal model, different power heating have been simulated to compute the thermal gradient. The total load has been given considering the resistance in each of the different area of the heater and not uniformly distributed throughout the heater path (previously described in the paragraphs 3.4.1 and 3.4.2). Thus, given a certain current and voltage values, the power heating has been achieved dividing the total area in three regions, as summarized in the table 13:

Table 13 Power heating simulated on the model

T [°C] Thermal Image	T [°C] Resistance	Voltage [V]	Current [A]	Total Power [W]	R4 Power [W]	R3 Power [W]	R2 Power [W]
36.8	40.9	10.41	0.011	0.12	0.07	0.04	0.01
59.9	60.4	15.52	0.016	0.26	0.15	0.08	0.03
70.1	69.9	17.60	0.019	0.33	0.19	0.10	0.03
86.1	85.5	20.69	0.022	0.45	0.26	0.13	0.05
97.9	97.7	22.82	0.024	0.54	0.32	0.16	0.06

5.2 Boundary conditions

To determine the thermal gradient, the boundary conditions, concerning the temperature of the spacers (T1, T2, T3) and the global heat exchange coefficients (h) have been modified considering that the convection coefficients depend on the temperature of the background and the measured temperature of the electrode. Starting from the procedure explained in the paragraph 3.4.3, the following parameters have been computed:

Table 14 Boundary condition parameters

T Resistance [°C]	h quartz crystal top [W/(m²K)]	h quartz crystal bottom [W/(m²K)]	h electrode top [W/(m²K)]	h electrode bottom [W/(m²K)]	T1 [°C]	T2 [°C]	T3 [°C]
40.9	18.52	18.52	16.07	14.65	18.5	21.5	19.6
60.4	21.86	21.86	19.19	17.60	29.2	33.5	32.1
69.9	23.09	23.09	20.30	18.63	31.7	37.4	34.9
85.5	24.83	24.83	21.82	20.01	33.8	39.9	36.2
97.7	26.04	26.04	22.84	20.93	38.8	47.0	43.7

5.3 Results

In the following, the results of the thermal gradient computations have been displayed considering its evolution along the electrode edge:

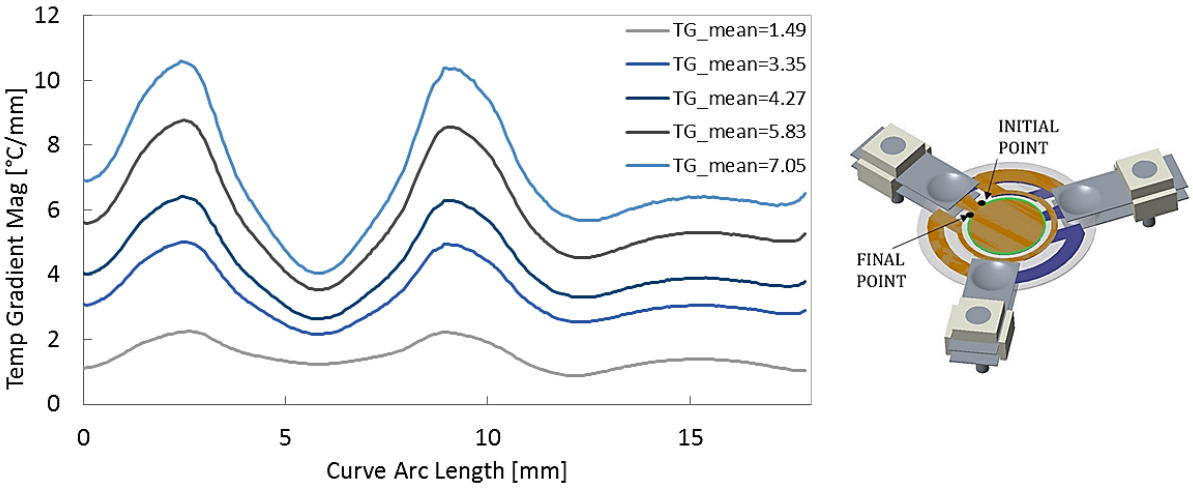

Figure 43 The average thermal gradient (TG_ mean) on the electrode edge.

In the Table 15, the numerical results are summarized:

Table 15 Thermal gradient and temperature results

Thermal gradient Mean [°C/mm]	Thermal gradient Min [°C/mm]	Thermal gradient Max [°C/mm]	T max [°C]	T min [°C]	T mean [°C]
1.49	0.88	2.25	43.8	38.2	42.0
3.35	2.16	5.02	67.5	55.8	64.0
4.27	2.63	6.42	77.9	63.2	73.6
5.83	3.54	8.77	93.9	74.1	88.1
7.047	4.04	10.60	106.6	83.1	99.8

Once determined the temperature and the thermal gradient, it has been possible to correlate such values with the frequency variation. The frequency variation (Δf) due to the thermal gradient has been computed subtracting from the frequency shift experimentally measured (sum of both contribute of the uniform temperature and the thermal gradient), the frequency variation due to the uniform temperature (obtained applying the equation of the polynomial regression $y = 0.0013x^3 - 0.1301x^2 + 3.4211x - 26.939$ in the Figure 16).

Table 16 Frequency variation due to the thermal gradient.

Thermal gradient Mean [°C/mm]	Thermal gradient Min [°C/mm]	Thermal gradient Max [°C/mm]	T [°C]	Experimental frequency variation [Hz]	Uniform temp frequency variation [Hz]	Thermal gradient frequency variation [Hz]
1.49	0.88	2.25	40.9	418.0	-15.7	**433.7**
3.35	2.16	5.02	60.4	1043.8	-8.6	**1052.3**
4.27	2.63	6.42	69.9	1181.9	20.5	**1161.3**
5.83	3.54	8.77	85.5	1694.5	127.0	**1567.5**
7.047	4.04	10.60	97.7	2235.8	277.7	**1958.1**

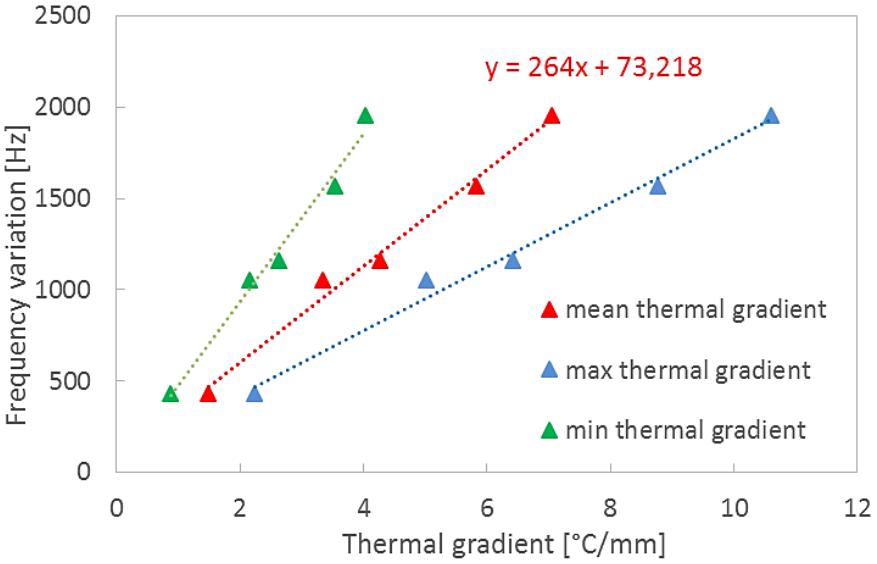

Figure 44 Frequency variation vs thermal gradient

Finally, to verify if the values are correlated, the correlation coefficients have been computed for the mean, the minimum and the maximum thermal gradient, by means of the following formula:

$$correlation(x,y) = \frac{\sum(x-\bar{x})(y-\bar{y})}{\sqrt{\sum(x-\bar{x})^2 \sum(y-\bar{y})^2}} \quad (5.1)$$

where x and y correspond to the thermal gradient values and the frequency variation due to the thermal gradient respectively; the $\bar{x}$ and $\bar{y}$ are the correspondent mean values. The correlation coefficient is a statistical relationship between two vectors of a given data (i.e. thermal gradient mean- frequency variation). The correlation coefficient can assume values in the range from −1 to +1, where +1 and -1 indicates that the two are linearly dependent while 0 express the condition of non-correlation. The obtained results are shown below:

Table 17 Correlation coefficients (CC)

CC mean_TG	CC min_TG	CC max_TG
0.995	0.993	0.994

Being all coefficients close to the unitary value, it can be concluded that frequency changes and all the investigated parameters are correlated.

5.4 Adjustment of the frequency variation due to the thermal gradient

To validate the correction procedure for the temperature gradient, the average temperature gradient has been computed by means of thermal analysis. Giving a defined power, the frequency variation has been experimentally measured. The results from the experimental activity are summarized in the Table 18:

Table 18 Results from the experimental activity

$\overline{T_{bk}}$[°C]	R[Ω]	T_R[°C]	V [V]	I [A]	Δf [Hz]	T_{ele} [°C]	T_{heat}[°C]
23.08	37.04	51.75	13.46	0.014	699.09	50.29	53.47

The thermal analysis has been performed on the model giving the following parameters, as computed in the paragraphs 3.4.2 and 3.4.3:

Table 19 Boundary conditions

h quartz crystal top [W/(m²K)]	h quartz crystal bottom [W/(m²K)]	h electrode top [W/(m²K)]	h electrode bottom [W/(m²K)]	T1 [°C]	T2 [°C]	T3 [°C]
20.57	20.57	18.00	16.49	26.45	30.62	28.91

Table 20 Thermal loads

Total Power [W]	R4 Power [W]	R3 Power [W]	R2 Power [W]
0.193	0.115	0.058	0.020

The results of the average thermal gradient has been computed below:

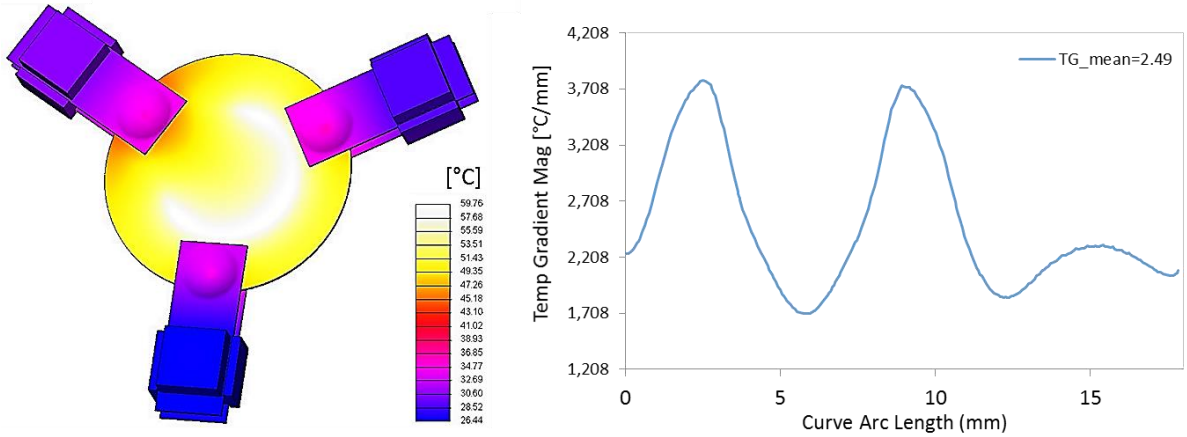

Figure 45 Average thermal gradient computation

Table 21 Numerical results from the thermal analysis

Thermal gradient Mean [°C/mm]	Mean temperature [°C]	Temperature measured from resistance [°C]
2.49	55.15	51.75

By using the thermal gradient vs frequency variation curve (Figure 46) the corresponding corrective factor has been identified. Thus, considering the frequency variation-thermal

gradient graph, entering with gradient 2.49 °C/mm, the frequency variation has been determined equal to 730.64 Hz, by using the linear regression coefficients:

$$\Delta f_{thermal\ gradient} = 264 \cdot 2.49 + 73.218 = 730.64\ Hz \tag{5.2}$$

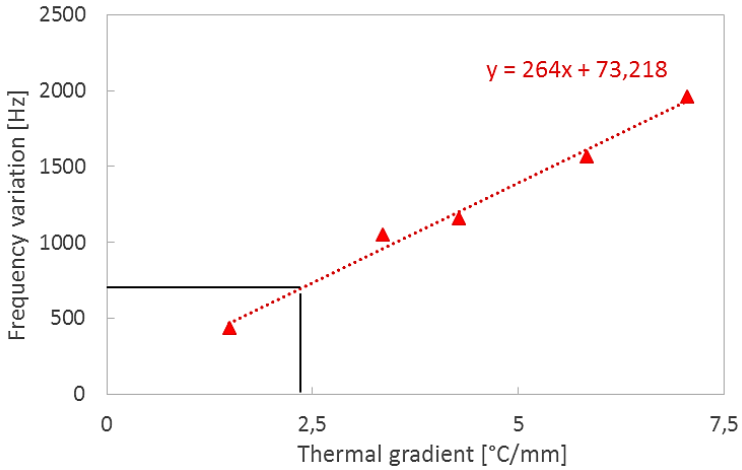

Figure 46 The corrective frequency variation with the mean thermal gradient equal to 2.49

Starting from the temperature value measured by the resistance deposited on the surface of the crystal, the corresponding frequency variation has been identified on the curve of the uniform temperature distribution. Knowing the frequency variation-uniform temperature trend, the value of 51.75°C has been used to get into the graph (Figure 47) and to determine the frequency variation in case of no thermal gradient. The result has been computed equal to -19.77 Hz.

$$\Delta f_{uniform\ temp} = 0.0013 \cdot\ 51.75^3 - 0.1301 \cdot\ 51.75^2 + 3.4211 \cdot\ 51.75 - 26.939 = -19.77\ Hz \tag{5.3}$$

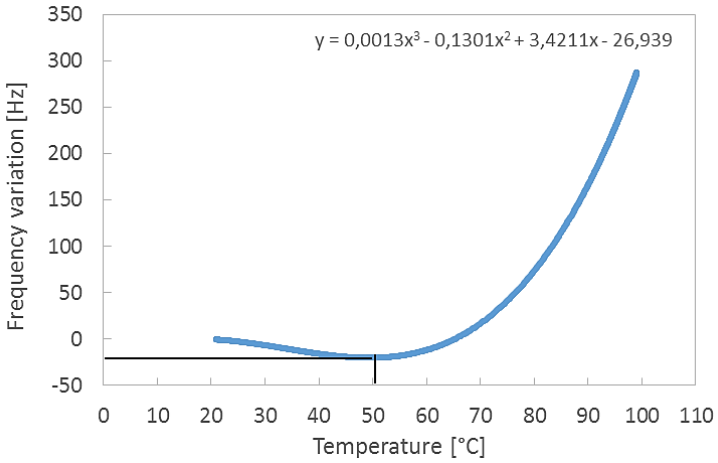

Figure 47 Frequency variation at uniform temperature.

Finally, adding the corrective frequency variation identified by means of the thermal gradient graph (Figure 46) with the one from the uniform temperature case (Figure 47), the following value has been obtained:

$$\Delta f_{predicted} = \Delta f_{thermal\ gradient} + \Delta f_{uniform\ temp} = 730.64 + (-19.77) = 710.87\ Hz \quad (5.4)$$

This procedure has been applied for different temperature values, identifying the corresponding corrective factor. Finally the percentage error has been computed following the formula explained below:

$$error\ \% = \frac{\Delta f_{experimental} - \Delta f_{predicted}}{\Delta f_{experimental}} \cdot 100 \quad (5.5)$$

The table 22 summarizes the results:

Table 22 Corrective factor for different temperature and the percentage error

Thermal gradient Mean [°C/mm]	T [°C]	Gradient frequency variation [Hz]	Uniform temp frequency variation [Hz]	Predicted frequency variation [Hz]	Experimental frequency variation [Hz]	Error [%]
2.49	51.75	730.64	-19.77	710.87	699.00	**-1.7 %**
3.36	59.63	959.79	-12.37	947.42	1031.57	**8.2 %**
4.00	65.44	1130.42	0.81	1131.23	1151.92	**1.8 %**
4.75	73.45	1326.93	32.97	1359.91	1370.07	**0.7 %**
4.7	76.42	1314.08	49.66	1363.74	1397.14	**2.4 %**
5.79	87.05	1601.57	134.82	1736.40	1748.55	**0.7 %**

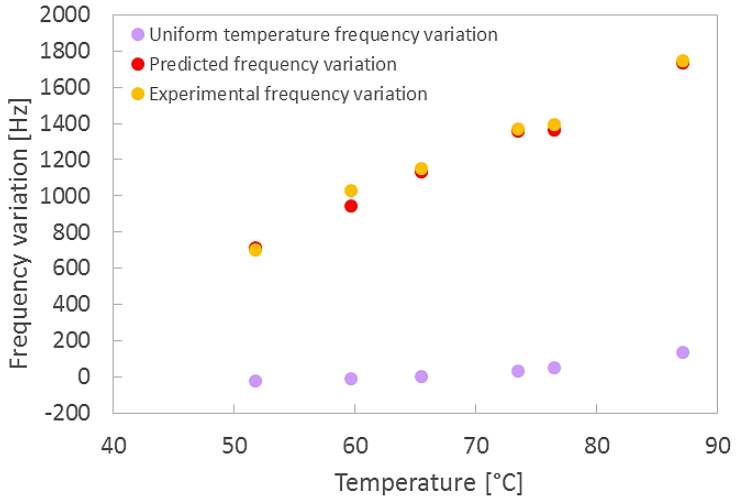

Figure 48 Corrective factor of the thermal gradient applied starting from the frequency variation of the uniform temperature. The results is compared with the values obtained experimentally.

It is noted that in the worst case at 60 °C, the error related to the frequency variation in the presence of the thermal gradient is reduced of 91.8 % while at 73.45 °C and at 87.05 °C the error is reduced by 99.3%. Thus, a sensitivity factor of the frequency with the temperature

gradient has been determined, enabling to perform a first order correction of the effect. The correction procedure has been implemented in a few cases and the residual error has been assessed in the range from -1 to +8 % of the original effect at temperature greater than 50°C.

5.5 Application of the corrective factor on a standard crystal

Since the analysis and correction of the thermal gradient effects has been carried out on the crystal on which the gold had been removed, that is not the kind of element normally used for a QCM, the same procedure has been repeated on a standard crystal (with the deposited gold). The crystal has endured the complete process i.e. its thermometer has been characterized performing the calibration inside the thermal bath, the non-uniform temperature effect on the frequency has been characterized under different heating power to the deposited resistor. Here below the results have been summarized:

5.5.1 Calibration of the QCM 5 film thermometer

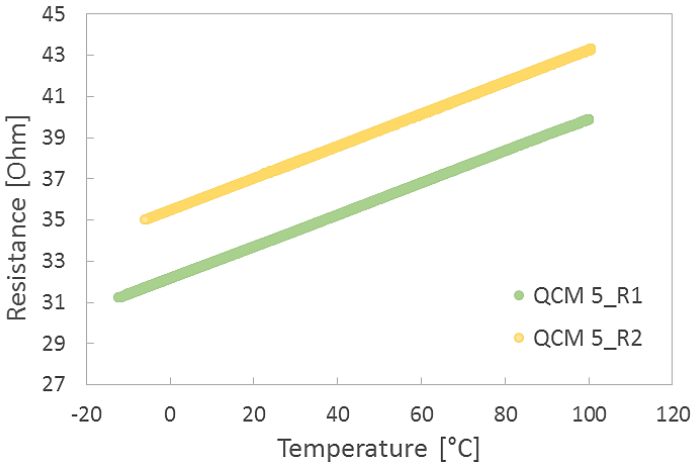

Figure 49 Calibration curve: Resistance vs Temperature of the deposited film (the heater and the RTD)

Table 23 Linear regression and standard deviation results

QCM	S [Ω/°C]	R_0 [Ω]	Linearity standard deviation [Ω]
5_R1	0.077	32.17	0.0116
5_R2	0.078	35.48	0.0075

Experimental results evidenced high linearity of the deposited thermometer, leading to an instrumental uncertainty of about 0.15°C and 0.09 °C (R1 and R2 respectively) with the linear model within investigated temperature range.

5.5.2 Non-uniform temperature effect on the frequency variation

In the Figure 50, the effect of the non-uniform temperature on the frequency variation has been shown. Different heating power have been generated by means of the deposited resistor on the crystal and the frequency variation has been measured by using the frequency counter Keysight 53220A. Five heating cycles have been performed to evaluate the repeatability. The curves do not overlapped each other perfectly. A repeatability standard deviation of 90 Hz has been identified. In particular, the points at low

temperatures assume very different values of the frequency variation. This can be justified by the deposit of contaminants on the surface of the crystal that determine a decreasing of the frequency [11]. Repeatability improves at high temperature due to the contaminants desorption. The results are shown in Figure 50, with the adopted third order interpolating polynomial.

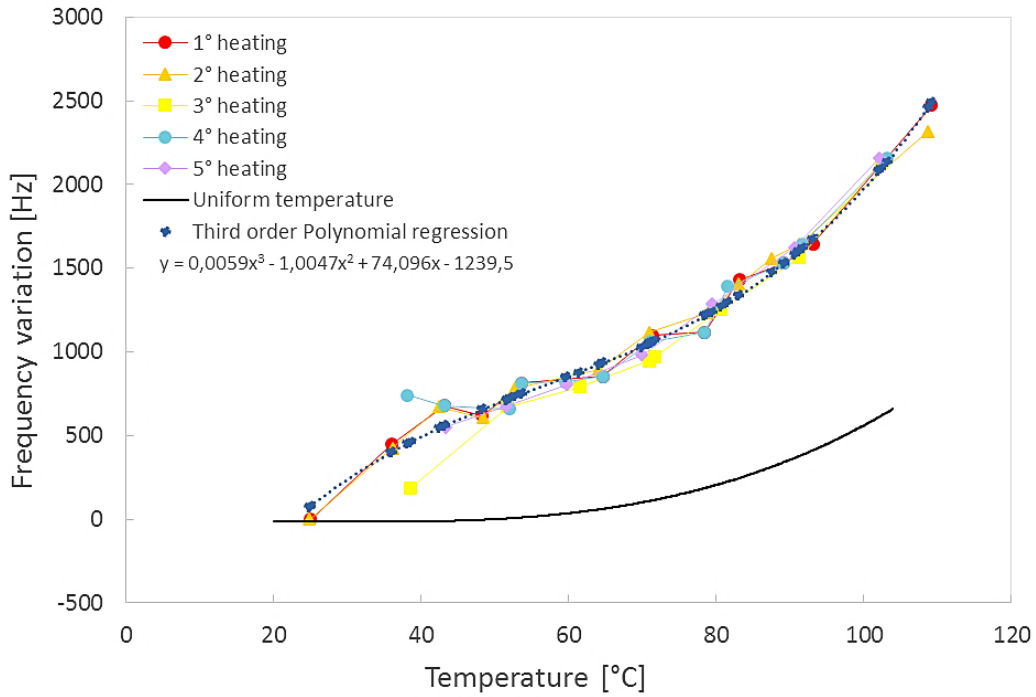

Figure 50 Frequency variation-temperature polynomial regression due to the uniform temperature and thermal gradient effects

Finally the non-uniform effect on the frequency variation has been compared with the uniform temperature effect, previously determined performing the test on the QCM 1 inside the vacuum chamber. The large difference between the two conditions is once again evident.

5.5.3 Thermal gradient effect correction

In order to compute the corrective factor of the thermal gradient effect, the thermal analysis has been performed simulating different heating power (as widely discussed in the paragraph 5.1). The low temperature data have been discarded due to the influence of deposited contaminants on the frequency variation. Table 24 summarizes the parameters.

Table 24 Power heating for the thermal analysis (first cycle heating)

T [°C] Resistance	Voltage [V]	Current [A]	Total Power [W]
52.02	3.0	0.069	0.207
59.61	3.5	0.078	0.272
64.59	3.7	0.082	0.305
71.11	4.0	0.089	0.355
78.44	4.4	0.095	0.419
81.57	4.5	0.098	0.441
89.17	4.8	0.103	0.496
91.72	5.0	0.106	0.529
103.15	5.5	0.114	0.625

Furthermore, the boundary conditions have been defined considering the temperature of the spacers and the global heat exchange coefficients (as described in the paragraph 3.4.3). The Figure 51 shows the prescribed temperature on the spacers and the radiation and convection conditions on the crystal, embedded in the global heating exchange coefficients.

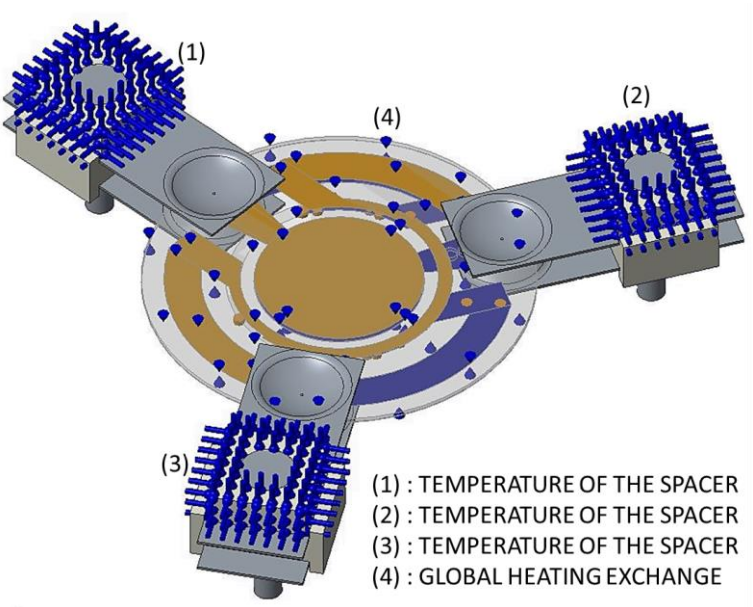

Figure 51 Boundary conditions in the thermal analysis

Table 25 Boundary conditions parameters (first cycle heating)

T Resistance [°C]	h quartz crystal top and bottom [W/(m²K)]	h electrode top and bottom [W/(m²K)]	T1 [°C]	T2 [°C]	T3 [°C]
52.0	21.94	17.77	27.7	28.0	27.1
59.6	23.17	18.80	28.4	28.7	27.7
64.6	23.79	19.30	29.4	29.9	28.4
71.1	24.48	19.86	29.5	30.1	28.7
78.4	25.46	20.62	30.6	31.4	29.7
81.6	25.69	20.79	30.4	30.8	29.5
89.2	26.42	21.35	30.8	31.6	32.7
91.7	26.78	21.61	31.7	31.9	30.8
103.2	27.84	22.37	32.4	33.12	31.6

The results of the thermal analysis in terms of average thermal gradient has been plotted in the Figure 52. Once determined the average temperature and the thermal gradient, they have been correlated with the frequency variation. This latter has been computed subtracting from the frequency shift, experimentally measured (sum of both contributions of the uniform temperature and of the thermal gradient), the frequency variation due to the uniform temperature. The results are summarized in the Table 26.

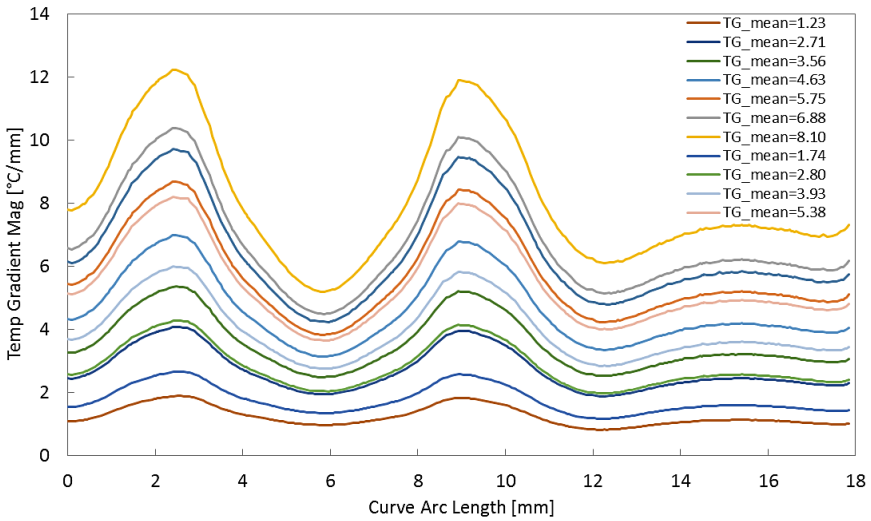

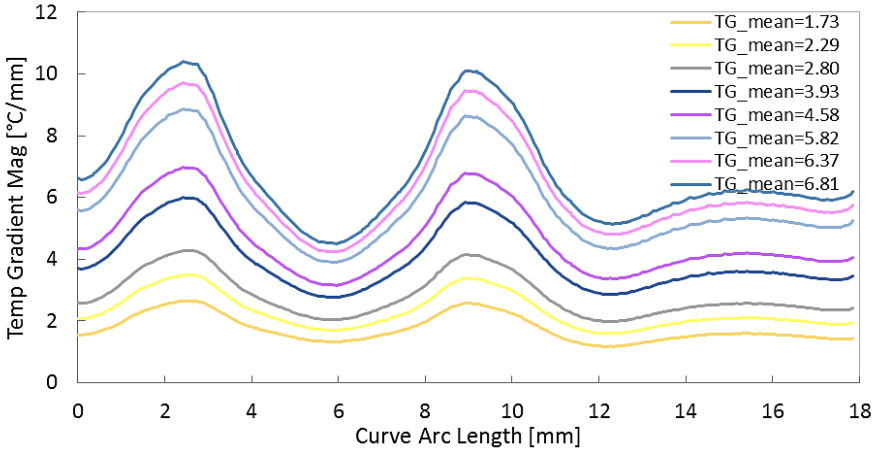

Figure 52 The average thermal gradient (TG_ mean) on the electrode edge (first heating cycle on the top and third heating cycle on the bottom)

Table 26 Frequency variation due to the thermal gradient

T [°C]	Thermal gradient Mean [°C/mm]	Experimental frequency variation [Hz]	Uniform temp frequency variation [Hz]	Thermal gradient frequency variation [Hz]
1°CYCLE				
52.02	2.71	632	5	627
59.61	3.56	792	33	759
64.60	3.93	854	61	793
71.11	4.63	1033	110	923
78.44	5.38	1117	185	932
81.57	5.75	1362	225	1137
89.17	6.37	1530	341	1190
91.72	6.88	1617	386	1231
103.15	8.10	2132	638	1494
2° CYCLE				
53.64	2.80	766	10	756
64.60	3.93	806	61	745
78.44	5.38	1069	185	884
89.17	6.37	1482	341	1142
3° CYCLE				
42.44	1.73	640	-12	652
52.79	2.80	754	7	747
64.11	3.93	863	58	805
70.97	4.58	1086	109	977
83.03	5.82	1374	245	1129
87.53	6.37	1528	313	1215
91.15	6.81	1609	376	1233
4° CYCLE				
51.75	2.70	671	4	667
61.45	3.66	792	43	749
70.85	4.67	947	108	839
80.65	5.76	1254	213	1041
91.25	6.94	1562	378	1184
102.39	8.21	2132	619	1513

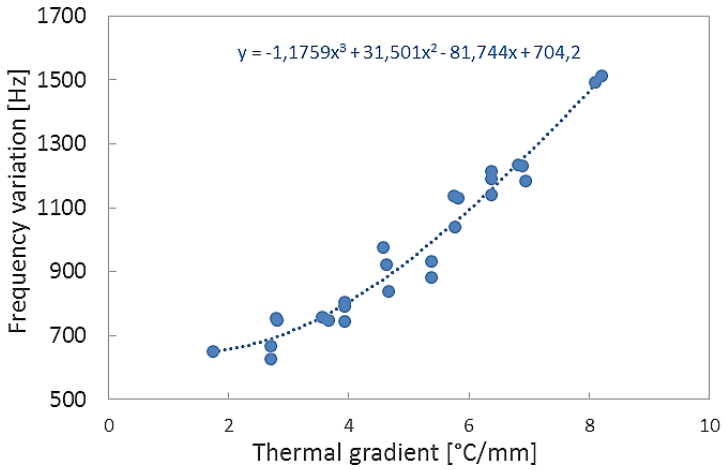

Figure 53 Frequency variation vs thermal gradient

The correlation coefficient for the mean thermal gradient fitting 3rd order polynomial was 0.964, the value is close to one but, as noticed before data dispersion was significant in these tests.

5.5.4 Application of the corrective procedure to experimental data

Finally, the effectiveness of the correction procedure has been verified with a new experimental campaign. By using the model of the thermal gradient effects i.e. the polynomial regression of the mean gradient values, along with that of the uniform temperature, (Figure 54), the frequency variation of the crystal heated with different power levels has been predicted (as explained in the paragraph 5.4).

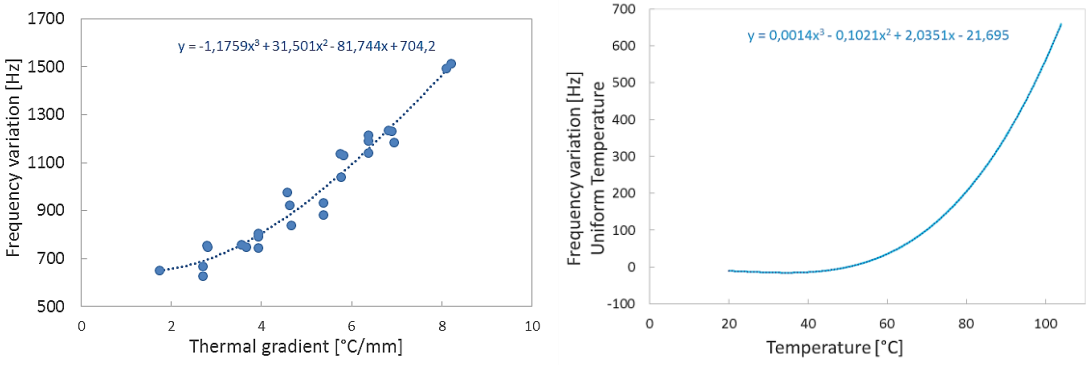

Figure 54 Polynomial regression to determine the corrective frequency variation (on the left) and the frequency variation-temperature trend due to the uniform temperature (on the right).

In order to perform the model validation, the frequency variation has been measured by the experimental activity, suppling different powers to the crystal resistor. Thermal analyses have been performed to compute the mean thermal gradient, reproducing the same conditions of the experimental activity. The results of the thermal analyses are displayed below:

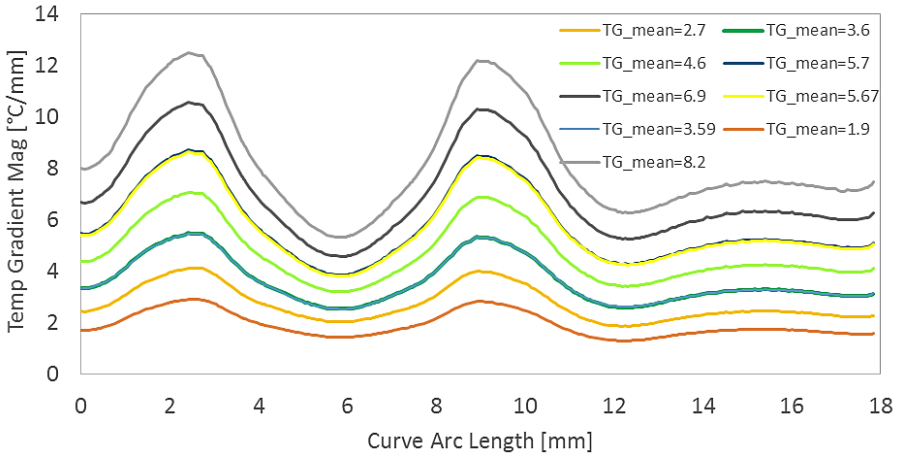

Figure 55 Mean thermal gradient results from the thermal analyses.

Eventually, the frequency variation has been computed and compared with the experimentally obtained values. The results and the residual error are shown in the Table 27:

Table 27 Corrective factor for different temperature and the percentage error

Thermal gradient Mean [°C/mm]	T [°C]	Gradient frequency variation [Hz]	Uniform temp frequency variation [Hz]	Predicted frequency variation Δf [Hz]	Experimental frequency variation [Hz]	Error [%]
1.904	43.3	654.64	-11.33	643.31	550.00	**16.9**
1.902	44.1	654.60	-10.39	644.21	522.12	**23.4**
2.701	51.5	690.08	3.61	693.69	675.00	**2.8**
3.206	56.1	727.17	18.19	745.36	798.07	**-6.6**
3.592	59.7	762.56	33.73	796.29	804.00	**-1.0**
3.594	60.5	762.73	37.74	800.47	789.00	**1.5**
4.245	66.6	834.85	74.67	909.53	896.14	**1.5**
4.644	69.9	886.12	99.62	985.74	983.00	**0.3**
5.667	78.9	1038.54	191.97	1230.52	1293.00	**-4.8**
5.717	79.5	1046.72	197.74	1244.46	1284.00	**-3.1**
5.963	82.5	1087.57	236.90	1324.47	1327.59	**-0.2**
6.932	90.7	1259.62	366.81	1626.43	1626.00	**0.03**
7.659	97.9	1397.65	514.71	1912.37	1791.47	**6.7**
8.200	102.1	1503.58	611.65	2115.23	2158.00	**-2.0**

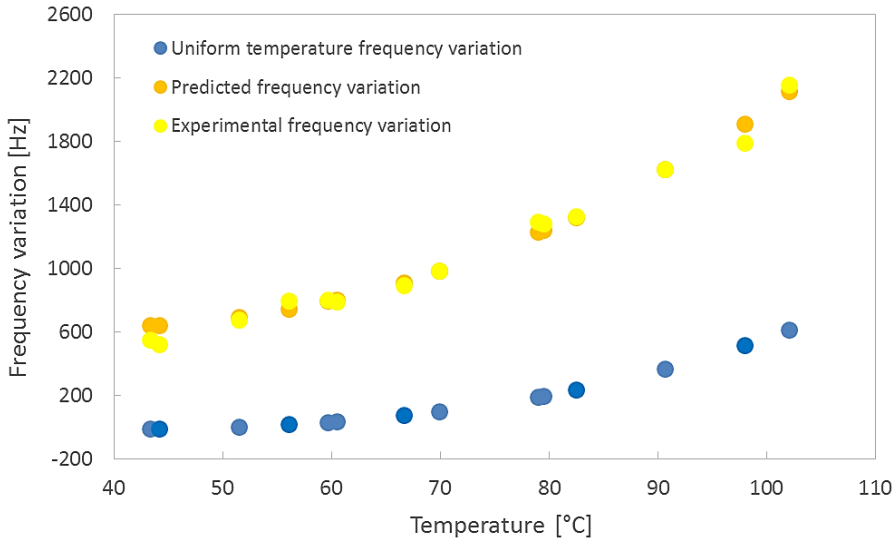

Figure 56 Corrective factor of the thermal gradient applied starting from the frequency variation of the uniform temperature. The results is compared with the values obtained experimentally.

It is noted that in the worst case at low temperature (between 40°C and 50 °C), the correction overestimates the real value of the frequency variation (measured experimentally) due to the uniform temperature and thermal gradient. The latter has been once again explained with the effect at low temperatures of deposited contaminants. As the temperature increases due to the thermal gradient, the frequency variation has been properly measured allowing to correct the effect of the gradient with residual errors smaller than 10%. In the range of 60-90°C, the error related to the frequency variation in the presence of the thermal gradient is always reduced by about 95%.

5.6 Derivation of the gradient from the power dissipated

The heat delivered by the heater on the crystal spread from heater area by thermal conduction on the crystal. The conduction in solids can be expressed writing the heat flux (i.e., the heat transfer rate per unit area normal to the direction of the gradient vector) q" is proportional to the temperature gradient:

$$q'' = -k\frac{dT}{dx} \tag{5.6}$$

where k is the thermal conductivity and is a material property. The minus sign is a consequence of the fact that heat is transferred in the direction of decreasing temperature. The Equation 5.6 is the one-dimensional form of Fourier's law of heat conduction. Recognizing that the heat flux is a vector quantity, a more general statement of Fourier's law can be written as:

$$q'' = -k\nabla T \tag{5.7}$$

where ∇ is the three-dimensional gradient operator and T is the scalar temperature field. From Equation 5.6 it is evident that the heat flux vector q" is proportional to temperature gradient [33] moreover the integral of the flow rate on a surface enclosing the heater shall provide the power dissipated on the heater.

According to the above considerations, a correlation between the average gradient on the electrode border and the power dissipated by the deposited heater might be expected. To verify this hypothesis the mean thermal gradients, computed performing five heating cycles, have been coupled with the heating power as shown in the Figure 57. The values have been interpolated using a linear regression obtaining a linearity standard deviation of 0.0265 [°C/mm].

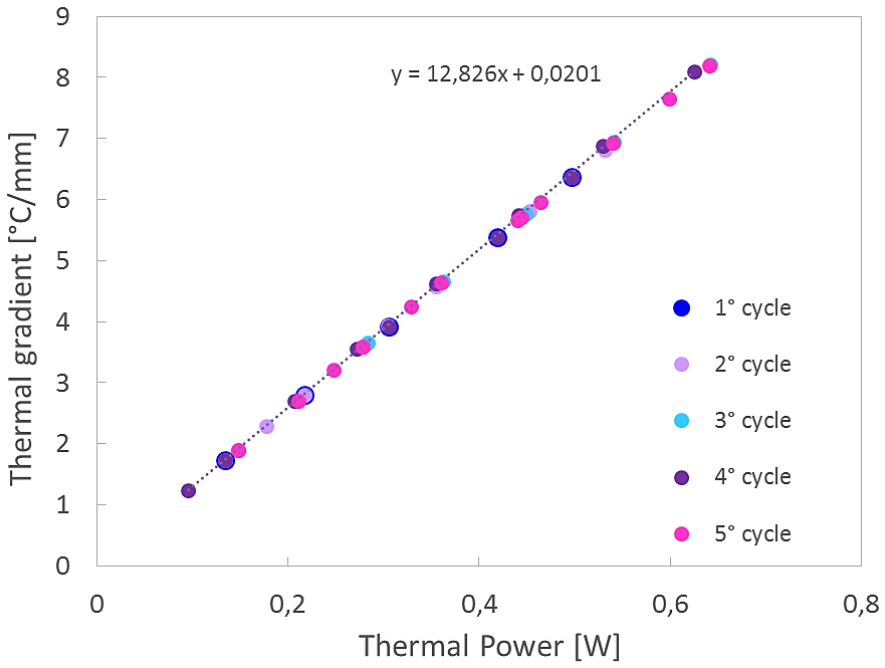

Figure 57 The temperature gradient vs the thermal power

This result is significant from a practical point of view because it allows to directly determining the thermal gradient from the thermal power supplied to the crystal resistor without having to perform every time a dedicated thermal analysis.

5.7 Conclusions

The corrective procedure of the thermal gradient has been developed on a modified crystal (without gold) where thermal mapping could be performed. The results of the application of the frequency variation correction, achieved through the linear regression of the frequency variation versus thermal gradient, combined with the model of frequency variation at uniform temperature led to residual errors in the range of 1 to 8 % of the original effect. The same procedure has been applied to a new crystal (with gold coated electrodes and the same cut angle of the crystal without gold). Using third order polynomials to model both the frequency variation due to uniform temperature and to thermal gradients, the achieved residual error is below 7 % in the temperature range above 50°C. Despite errors above 20% have been observed at lower temperatures this has been attributed to desorption of contaminants that is expected at the switch-on of the heaters.

6 CONCLUSIONS

This work has confronted with the development of a QCM for dust and molecular contamination monitoring. The problem of measuring dust depositions with a QCM has proved to be still an open one. The solid particles adhesion to the crystals is a critical issue and it has been proved that the deposition of "normal dust" of the kind collected in ducts of air conditioning systems leads to erratic measurements. Some improvements have been achieved increasing the sticking properties of the crystal surface but the problem has not been solved and this kind of application will likely be feasible only if a dimensional selection is performed before the QCM.

Concerning the application for molecular contamination the QCM under development was characterized for an innovative crystal configuration that includes heaters and thermometers deposited on the surfaces as film resistors. The great advantages of the new configuration in terms of accuracy in the temperature measurement and control brought new issues related to significant thermal gradients on the crystal. The temperature-frequency characterization of the quartz crystal microbalance required the analysis not only of the effect of different uniform temperatures of the crystal that was the state of the art but also the identification of the effect of the temperature gradients. The innovative built-in heater and temperature sensor gave the chance of measuring the crystal temperature right at the sensing area i.e. on the electrode border with minimum error, allowing to perform the calibration of the oscillating frequency vs temperature with high accuracy. Crystal calibration has been performed within different environments, a temperature-controlled enclosure in air and in vacuum. Qualitative agreement with the literature models has been evidenced, while matching is not expected because of the dependency on the crystal manufacturing characteristics. Repeatability issues led to highlight the sensitivity of the instrument to the contamination that was evidenced even in medium vacuum environment.

The analysis has then focused on the crystal frequency behavior under temperature gradients. The results of the thermal gradient effect on the frequency variation have been compared with the uniform temperature-frequency variation relationship. It has been evidenced that, with the adopted configuration, the effect of thermal gradients is by far more relevant than that of the average temperature.

The temperature field on the crystal surface was measured with a thermal mapper. The measurement on the original quartz crystals was not feasible because of the gold plating of the electrodes so, the gold coating was removed and the emissivity of the underlying metal measured. The thermal image processing allowed determining the temperature distribution and the thermal gradients at the electrode border. The information nevertheless was affected by the low spatial resolution of the thermal image and the gold coating removal.

To identify the temperature field on the crystal surface of a standard QCM crystal, a thermal model has been developed. The model of the gold removed crystal was first validated by comparing the predicted temperatures with those measured through the thermal mapper. The predicted temperatures were quite close to the measured ones with maximum errors

on the electrode temperature below 1 °C. Thus, the validated mathematical model was used to evaluate the thermal gradients on the crystals.

Finally, in order to correlate the temperature gradient with the frequency variation, different thermal loads and the boundary conditions, used during the experimental activity, were simulated assessing the temperature gradients as a results. A sensitivity factor of the frequency with the temperature gradient has been computed, enabling to perform a first order correction of the effect. The correction procedure has been implemented in a few cases and the residual error assessed. Despite this was just the first attempt of correcting the gradient effects, the results was promising being the residual error in the range of 1 to 8 % of the original effect.

The correction procedure has then been implemented also on a standard crystal. The correction procedure allowed achieving residual errors below 7% for temperatures above 50°C. The correction procedure was quite ineffective at temperatures in the 40°C range where a low repeatability of the frequency measurements was observed and the correction procedure led to errors up to 20%. The low repeatability nevertheless could be addressed to contaminants deposited on the crystals that are released at the switch on of the heaters. Performing the tests under high vacuum is expected to improve the measurements repeatability and therefore the accuracy of the whole procedure, nevertheless, the achieved results allow to be confident that the proposed QCM can be used for TGA analysis at high temperature and with fast temperature rise enabled by the new crystals configuration.

ANNEX A

```
clc
clear all
close all

Data= xlsread('Data.xlsx');
Temp= Data(:,1);
Fc=Data(:,2);

[P,S]=polyfit(Temp,Fc,3)
[Y,delta]=polyval(P,Temp,S)

figure
plot(Temp(1:14),Fc(1:14),'mo')
hold on
plot(Temp(15:21),Fc(15:21),'bo')
hold on
plot(Temp(22:28),Fc(22:28),'co')
hold on
plot(Temp,Y,'k*')

legend('Th-bb 3cm 1 cycle','Th-bb 3cm 2 cycle','Th-bb 3cm 3
cycle','Polynomial regression','Location','SouthEast')
xlabel('Infrared camera temperature [°C]')
ylabel('Fc')
```

ANNEX B

```
clc
clear all
close all

%% TEMPERATURE
Tth_C= xlsread('Data25.xlsx');
Tth_K= Tth_C(:,:)+ 273.15;
Tbk= 23.163+273.15;

%% CORRECTIVE FACTOR FOT THE INFRARED CAMERA
Fc=(Tth_C.^3* 4.70554E-07+ Tth_C.^2*(-0.000107803)+
Tth_C.*(0.008308522)+0.801685515);

%% REAL TEMPERATURE
eps_elettrodo = 0.254194;
eps_heater=0.629526;
eps_gold=0.03;

Tth_C_ele_new=((((Fc.*Tth_K.^4)-((1-eps_elettrodo)*
Tbk^4))/(eps_elettrodo)).^(1/4))-273.15;
Tth_C_ele_new_zoom=Tth_C_ele_new(158:163,62:68);
Th_C_medio_e=mean(mean(Tth_C_ele_new_zoom))
Tth_C_max_e=max(max(Tth_C_ele_new_zoom))
Tth_C_min_e=min(min(Tth_C_ele_new_zoom))

Tth_C_heater_new=(((Fc.*Tth_K.^4)-((1-eps_heater)*
Tbk^4))/(eps_heater)).^(1/4)-273.15;
%Tth_C_heater_new(158:163,62:68)=Tth_C_ele_new_zoom;
Tth_C_heater_new_zoom=Tth_C_heater_new(143:150,77:79);
Th_C_medio_h=mean(mean(Tth_C_heater_new_zoom))
Tth_C_max_h=max(max(Tth_C_heater_new_zoom))
Tth_C_min_h=min(min(Tth_C_heater_new_zoom))
xlswrite('Th_C_risultati.xlsx',[Th_C_medio_e,Tth_C_max_e,Tth_C_m
in_e],1)
xlswrite('Th_C_risultati.xlsx',[Th_C_medio_h,Tth_C_max_h,Tth_C_m
in_h],2)
for ii=1:320
    for jj=1:240
if(Tth_K(ii,jj)<305)
    Tth_C_new(ii,jj)=(((Tth_K(ii,jj).^4)-((1-eps_gold)*
Tbk^4))/(eps_gold)).^(1/4)-273.15;
elseif (Tth_K(ii,jj)>306 && Tth_K(ii,jj)<333)
    Tth_C_new(ii,jj)=(((Fc(ii,jj).*Tth_K(ii,jj).^4)-((1-
eps_elettrodo)* Tbk^4))/(eps_elettrodo)).^(1/4)-273.15;
elseif (Tth_K(ii,jj)>335)
    Tth_C_new(ii,jj)=(((Fc(ii,jj).*Tth_K(ii,jj).^4)-((1-
eps_heater)* Tbk^4))/(eps_heater)).^(1/4)-273.15;
end
    end
end
```

```
figure(1)
image(real(Tth_C_new(:,:))','CDataMapping','scaled')
axis image
colormap Autumn
cmap = colormap;
newcmap = cmap(end:-1:1,:);
colormap(newcmap)
h = colorbar;
h.Label.String = 'Temperature';
title('Temperature mapping for the electrode')
xlabel('X Pixels');
ylabel('Y Pixels');
hold on
rectangle('Position',[158 62 5 6]);


figure(2)
image(Tth_C_ele_new_zoom(:,:)','CDataMapping','scaled')
axis image
colormap hot
cmap = colormap;
newcmap = cmap(end:-1:1,:);
colormap(newcmap)
h = colorbar;
h.Label.String = 'Temperature';
title('ZOOM electrode')
xlabel('X Pixels');
ylabel('Y Pixels');
```

ANNEX C: Analysis of the QCM sensitivity to solid particles deposition

In parallel, the activity has been focused on the applicability of the QCM to measure the deposition of solid particles of different size. Some issues related to the solid contaminants measurement have been identified from literature review:

1. the dependency of the crystal resonance frequency on the vibration amplitude and the particles size [34]
2. a preliminary indication that the 10 MHz QCM properly detects solid particles with size ranging from 0.05 to 0.5 μm (not fully assessed)
3. the necessity to control the distribution of the particles on the crystal surface,
4. the effective mass dependence on the sticking of the particles to the crystal.

From the literature [35], it was found that the 10 MHz QCMs work properly with grain sizes smaller than 0.5 μm nevertheless, recent studies have demonstrated that particles size up to 5 μm could be measured when using sticking coatings on the QCM. Since the previous statement was not been fully assessed and all the literature studies were based on synthetic spherical particles of uniform size, it was decided to verify the applicability limits of the 10 MHz microbalance on different kind of "normal" dust. The used dust was obtained from the deposits in air conditioning ducts, the choice was linked to the possible usage of the QCM for the monitoring of this kind of phenomenon. The granulometric analysis of the samples has been performed by using an optical microscope. From the image processing the dimensions of the particles deposited on the surface evidenced a mean diameter of 10.72 μm with a standard deviation of 9.4 μm. Two examples of the microscope images are shown below.

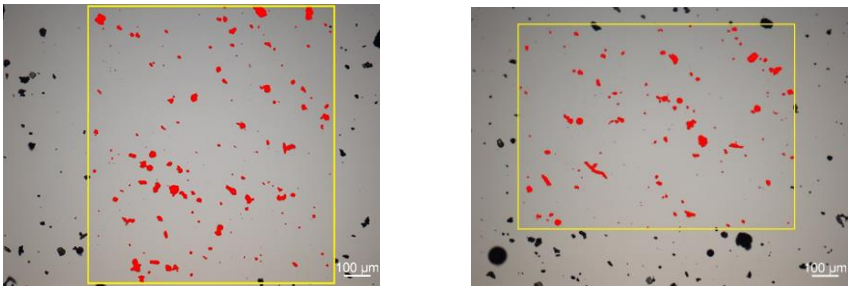

Figure 58 Particle samples analyzed by using the optical microscope.

The analyzed samples had therefore dimensions greater than the nominal limit of 5 μm, and the tests on the 10 MHz QCM device showed that the frequency was not affected by the mass deposition of this kind of dust.

The activity therefore proceed considering a 5 MHz QCM that according to literature studies, should be able to detect larger particles. A fixed amount of powder was deposited on the QCM using a purposely built ventilation duct. According to the Sauerbrey equation, under the hypothesis of a homogeneous film deposition, the expected frequency's decrease had been computed around 5-6 KHz.

$$\Delta f = -\frac{2f_0^2}{A\sqrt{\rho_q \mu_q}}\Delta m = -\frac{2(5\ 10^6)^2}{\sqrt{2.648\ \cdot 2.947 \cdot 10^{11}}} = -5660\ Hz$$

During the test, the frequency of the QCM has been monitored considering different lengths in terms of time and different speed of the fan. Analyzing the results reported in Figure 59, the frequency shifts are not significant and cannot be correlated to the deposition of the powder.

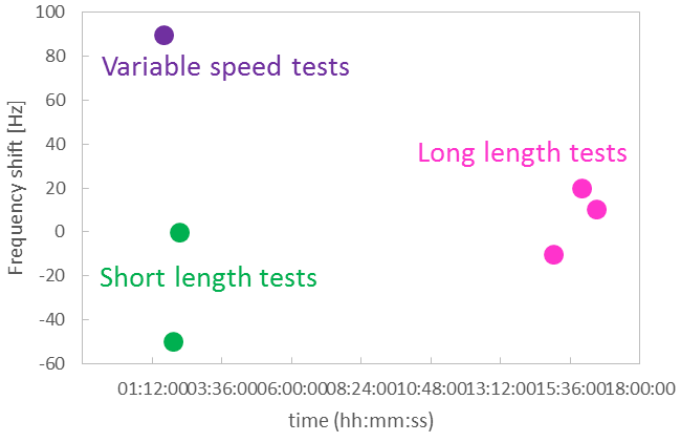

Figure 59 Frequency shift vs time

The QCM behavior in the test condition is far from the expected one. Two hypothesis have been formulated:

- the particle size is too widely distributed ad large particles has an effect opposed to the small ones leading to a sort of compensation
- the powder deposition occurs, but the hypothesis of homogeneous film is not fulfilled, thus the frequency shift does not follow the Sauerbrey equation

In order to improve the adhesion of the powder [36], the dust has been filtered (Figure 60) and a layer of grease (Apiezon N Grease, thickness 160 nm) has been deposited on the surface of the crystal. The grease layer make the powder particles fixed to the crystal in order to behave as one film. In that case, the QCM detects the mass deposition but the value of the frequency shift is one order below to the results of the Sauerbrey equation.

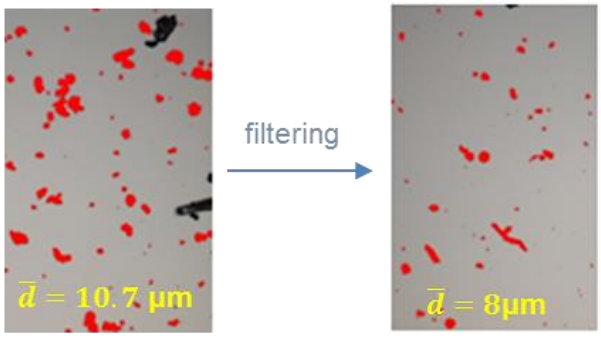

Figure 60 Particles dust filtering

Table 28 Frequency variation detection

TEST	f [MHz] before deposition	f [MHz] after deposition	Frequency variation [Hz]
1	4.964771	4.964660	111
2	4.964906	4.964602	304
3	4.964914	4.964703	211
4	4.965104	4.964998	106
5	4.965008	4.964905	103
6	4.963305	4.962834	471
Mean value	4.964668	4.964467	217.7
St.dev.rel	1.36E-04	1.64E-04	6.77E-01

The conclusion of this preliminary investigation led to conclude that the measurement of the deposition of solid particles with the QCM deserves a dedicated study. Out of the literature studies it is necessary to extend the knowledge from the behavior in laboratory conditions with monodisperse particles with controlled shape to “field conditions” with mixture of different particles in terms of size, composition and shape. The activity performed, though limited, has evidenced that the behavior cannot be simply derived from the existing studies.

References

[1] C. O'Sullivan and G. Guilbault, Commercial quartz crystal microbalances- theory and applications, Biosensors and bioelectronics, 1999, August 4.

[2] R. Ramus, Alpha Quartz, December 1989.

[3] V. E. Bottom, Introduction to quartz crystal unit design., Van Nostrand Reinhold, 1982.

[4] Vannucci, Anisotropia: analisi e metodi di rappresentazione, Pisa: Materiali Compositi, 2008.

[5] R. Bechmann, A. Ballato and T. J. Lukaszek, Higher-Order Temperature Coefficients of the Elastic Stiffinesses and Compliances of Alpha-Quartz., 1962.

[6] P. Raddani, Quartz Crystal Microbalance: temperature effects analysis, 2015.

[7] “http://www.treccani.it/enciclopedia/piezoelettricita,” [Online].

[8] Curie and Curie , An oscillating quartz crystal mass detector, Rendu 91, pp. 294-297, 1880.

[9] B. Capelle, Mode Shape Analysis Techniques Using Synchrotron X-ray Topography, 44th Annual Symposium On Frequency Control, pp. 416-423, 1990.

[10] G. Sauerbrey, Use of quartz vibration for weighing thin films on a microbalance., J.Physik, 1959.

[11] C. Lu, Mass determination with piezoelectric quartz crystal resonators, Journal of Vacuum Science Technology. 12, pp. 578-583, 1974.

[12] S. Martin , S. Senturia, G. Frye and A. Ricco, Effect of Surface Roughness on the Response of Thickness-Shear Mode Resonators in Liquids, Analytical Chemistry 65, pp. 2910-2922., 1993.

[13] H. Packard, Fundamentals of Quartz Oscillators - Application Note 200-2, U.S.A: Hewlett Packard, 1997 .

[14] K. Haruta and W. J. Spencer, X-ray Diffraction Study of Vibrational Modes, 20th Annual Symposium on Frequency Control, pp. 1-13., 1966.

[15] CCIR, Standard Frequency and Time Signals (Study Group 7), U.S.A, 1990.

[16] T. Meeker and J. R. Vig, The Aging of Bulk Acoustic Wave Resonators, Oscillators and Filters, 45th Annual Symposium on Frequency Control, 1991.

[17] J. A. Kusters, Resonator and Device Technology, Precision Frequency Control, Volume I, pp. 161-183., 1985.

[18] A. Ballato and J. Vig, Static and Dynamic Frequency-Temperature Behavior of Singly and Doubly Rotated, Oven-Controlled Quartz Resonators, 32nd Annual Symposium on Frequency Control, pp. 180-188., 1978.

[19] R. L. Filler, The Acceleration Sensitivity of Quartz Crystal Oscillators: A Review., IEEE Transactions on Ultrasonics, Ferroelectrics, and Frequency Control, 35(3), pp. 297-305., 1988.

[20] B. R. Capone, A. Kahan, R. N. Brown and Buckmelte, Quartz Crystal Radiation Effects, 1970: IEEE Trans. Nuclear Sci., Volume 17, pp. 217-221..

[21] J. R. Vig and F. L. Walls, Fundamental Limits on the Frequency Instabilities of Quartz Crystal Oscillators, IEEE Int'l Frequency Control Symposium, pp. 506-523, 1994.

[22] J. SEKLER , A. ZUMSTEG and E. HINTERMANN HANS, “Piezoelectric contamination detector”. Patent CH-662421-A5.

[23] N. Gufflet, Quartz crustal resonators- Brief overview -.

[24] D. Scaccabarozzi, B. Saggin, E. Palomba, A. Longobardo and E. Zampetti, Thermo-mechanical design and testing of a microbalance for space applications, Advances in Space Research, 6 September 2014..

[25] D. Scaccabarozzi, B. Saggin, M. Magni, M. Tarabini, E. Zampetti, F. Dirri, A. Longobardo, E. Palomba, J. Alves and A. Tighe, Characterization of thermally controlled quartz crystal microbalances, Metrology for Aerospace (MetroAeroSpace) IEEE, 2016.

[26] E. C. Series, Fundamentals of Quartz oscillators.

[27] E. O. Doebelin, Misure e incertezza di misure. In: Strumenti e metodi di misura, Strumenti e metodi di misura. Milano: McGraw-Hill, pp. 61-98, 2008.

[28] F. E. Fowle, The Non-Selective Transmissibility of Radiation Through Dry and Moist Air, Astrophysical Journal, Volume 38, pp. 392-406, 1919.

[29] M. F. Santos, E. Fujiwara, F. D. de Paula and C. K. Suzuki, Opacity measurements on quartz and its influence on silica glass properties, International Journal of Mineral Processing, Volume 124, pp. 141-144., 2013.

[30] I. G. Ltd, Heat transfer by free convection and radiation – simply shaped bodies in air and other fluids, ESDU 77031., 1978.

[31] J. Vig, QUARTZ CRYSTAL RESONATORS AND OSCILLATORS For Frequency Control and Timing Applications - A TUTORIAL, Fort Monmouth, NJ, USA: US Army Communications-Electronics Research: Development & Engineering Center, 2004.

[32] A. Longobardo, E. Palomba , F. Dirri and D. Scaccabarozzi, BB Test Report: TN 4300, Milano: Politecnico di Milano, 2015.

[33] W. R. Rohsenow, J. P. Hartnett and Y. I. Cho, Handbook of heat transfert, MCGRAW-HILL, 1998.

[34] Z. Haifeng and L. Pouhua , Experimental Study of Thickness-Shear Vibration of AT-Cut Quartz Resonators Loaded with Microparticles, IEEE Transactions on Ultrasonics, Ferroelectrics, and Frequency Control, 2011.

[35] Z. Qiliang , L. Ryszard M. and P. Kambiz , The Study of an Interaction of Solid Particles with Various Surfaces Using TSM Sensors, IEE transactions on ultrasonics, ferroelectrics, and frequency control, 2006.

[36] E. Vittorias, M. Kappl, B. Hans-Jürgen and D. Johannsmann, Studying mechanical microcontacts of fine particles with the quartz crystal microbalance, Powder Technology, 2010.